ARTICLE

https://doi.org/10.1590/2317-4889202320220068

BJGEO Brazilian Journal of Geology

Crustal growth in the northeast portion of the Rhyacian Bacajá domain, SE Amazonian craton, based on U-Pb, Lu-Hf, and Sm-Nd data

Lucas Baía Magalhães[1]*, Moacir José Buenano Macambira[2], Edesio Maria Buenano Macambira[3], Paulo dos Santos Freire Ricci[3]

Abstract

The Bacajá domain, southeastern Amazonian craton, comprises Mesoarchaean and Siderian terrains reworked during the Transamazonian cycle. Combined analyses of zircon LA-ICP-MS U-Pb and Lu-Hf with whole-rock Sm-Nd from the northeast portion of this domain made it possible to propose an evolutionary sequence between ca. 2.60 and 2.06 Ga. Gneisses with an igneous protolith age of 2630±15 Ma show negative signatures ($\varepsilon Hf_{(t)}$ = -0.3 to -1.7 and $\varepsilon Nd_{(t)}$ = -3.08 to -2.98) and a Mesoarchaean formation (Hf-T_{DM}^{C} and Nd-T_{DM} model ages range from 3.0 to 3.2 Ga). Rhyacian granite genesis lasted about 40 million years (2.10–2.06 Ga) and was divided into two magmatic periods. The first is represented by deformed granitoids with zircons yielding crystallization ages between 2.10 and 2.09 Ga and model ages (Hf-Nd) at about 2.5 Ga. The second event is represented by granitoids with preserved magmatic texture, crystallization ages of 2.06 Ga, and Siderian model ages (Hf-Nd) of around 2.3 Ga. The overall Hf isotopic analyses of this Rhyacian granite genesis exhibit a spread of $\varepsilon Hf_{(t)}$ values between 1.8 and -2.9, which show a probably underestimated mantle-derived contribution in this period.

KEYWORDS: U-Pb, Lu-Hf and Sm-Nd geochronology; Transamazonian cycle; Bacajá domain; Amazonian craton.

INTRODUCTION

The northern portion of the Amazonian craton comprises a Paleoproterozoic mobile belt reworked during the Transamazonian cycle (Tassinari and Macambira 2004). The southeastern part of this mobile belt, known as the Bacajá domain (BJD) (Fig. 1), is considered a key area for understanding crustal growth of this region. Such domain contains Siderian registers, scarce through all the Amazonian craton; it borders the Carajás block that is not affected by the Transamazonian cycle and shows several magmatic and deformational episodes that are still not very well characterized.

The BJD comprises a large volume of deformed granitoids and, to a lesser extent, granulites, gneisses, and metavolcano-sedimentary sequences. Isotopic data were mainly obtained from whole-rock Sm-Nd and Pb-evaporation on zircon (e.g. Barros *et al.* 2007, Vasquez *et al.* 2008a, Macambira *et al.* 2009, Macambira and Ricci 2013). These isotopic data, structural trends, lithostratigraphy, and geophysical features have made possible to reveal that the BJD is a Mesoarchaean to Siderian (3.00–2.30 Ga) terrain reworked during the Rhyacian orogenies and linked to the Transamazonian cycle (2.26–2.05 Ga) (Vasquez *et al.* 2008a, Macambira *et al.* 2009). This cycle was an important rock-forming event in the South American Platform, and it is detailed in Rhyacian stages on the BJD.

At least three distinct stages are inferred for the Rhyacian orogenies in the BJD. Vasquez *et al.* (2008b) and Macambira *et al.* (2009) have revealed that the oldest stage of ca. 2.2 Ga comprises granitoids with $\varepsilon Nd_{(t)}$ significantly negative and Nd-T_{DM} predominantly Mesoarchaean. They were formed in continental arcs at the margin of an Archaean continent. At about 2.1 Ga, granitogenesis appears as the main event, correlated with other regions, as in the Guiana Shield (e.g. Vanderhaeghe *et al.* 1998). These granitoids were emplaced in a continental margin linked to the collision climax of this cycle (Vasquez *et al.* 2008a). The final stage occurred between 2.09 and 2.06 Ga, and it is represented by granitoids and charnockites, some with preserved igneous textures (Barros *et al.* 2007, Macambira and Ricci 2013). $\varepsilon Nd_{(t)}$ spread from positive to negative values, and model ages (Nd) vary from Neoarchaean to Siderian. This final magmatic event is interpreted as the product of mixing processes (juvenile and crustal components).

In this study, we present the first data of integrated U-Pb, Lu-Hf, and Sm-Nd isotope data obtained on zircon and whole rock of Archaean gneisses, Rhyacian granitoids, and granulites from the northeastern portion of the BJD. The purpose of the study was to elucidate crustal growth from this domain.

[1]Programa de Pós-Graduação em Geologia e Geoquímica, Instituto de Geociências, Universidade Federal do Pará – Belém (PA), Brazil. E-mails: lucasb.mag@gmail.com, lucas_baia@hotmail.com

[2]Isotope Geology Laboratory, Instituto de Geociências, Universidade Federal do Pará – Belém (PA), Brazil. E-mail: moamac@ufpa.br

[3]Brazilian Geological Service – Belém (PA), Brazil. E-mails: edesio.macambira@gmail.com, paulo.ricci@cprm.gov.br

*Corresponding author.

It involves a discussion of the Archaean records, features from the Rhyacian granitogenesis, related with the Transamazonian cycle, and the event of high-grade metamorphism that affected that region.

GEOLOGY OF THE NE BACAJÁ DOMAIN

Orthogneisses, granulites, granitoids, and metavolcano-sedimentary sequences were mapped in the BJD (Table 1, Fig. 2) (e.g. Santos 2003, Faraco *et al.* 2005, Vasquez *et al.* 2008b, Macambira *et al.* 2009, Besser 2012, Macambira and Ricci 2013). In the northeastern part, orthogneisses were included in an Archaean unit called the Aruanã Complex, and the granitoids were divided between three units: Bacajaí Complex, Arapari, and João Jorge intrusive suites (Macambira and Ricci 2013).

The Aruanã Complex occurs in the northern portion of the BJD, which is crossed by important sets of NE-SW strike-slip faults and NW-SE foliations, identified through aero-geophysical surveys carried out by the Geological Survey of Brazil (CPRM) (Fig. 2). This unit mainly consists of orthogranulites with subordinate mobilized granitic material, and granitic pegmatites (Macambira and Ricci 2013). Barros and Besser (2015) identified banded metagranitoids and orthogneisses in the amphibolite facies. Although the mineral assemblage of the rocks from this complex would appear to indicate the amphibolite facies, the granoblastic texture suggests a higher degree of metamorphism (granulitic facies), as proposed by Macambira and Ricci (2013). These authors also presented geochemical data that point to an enrichment in large-ion lithophile elements (LILE) when compared with high-field strength element (HFSE) contents, indicating calcic-alkaline magmatism generated in a continental margin. Besser (2012) also obtained calcic-alkaline affinity and proposed a volcanic arc or sin-collisional environment for these rocks. Vasquez *et al.* (2008c) obtained an age of 2606 ± 4 Ma, interpreted as the igneous protolith crystallization age (Pb-evaporation in zircon method). Near Pacajá town, mobilized granitic materials were dated by Macambira and Ricci (2013) by the same method. Zircon crystals show a low Th/U ratio and yielded an age of 2.1 Ga, interpreted as related to a possible metamorphic event. To the west, Barros and Besser (2015) analyzed a metagranitoid that yielded an age of 2.6 Ga by zircon Pb-evaporation.

The Bacajaí Complex is composed of enderbites, charno-enderbites, and granitoids crossed by NE-SW strike-slip faults and NW-SE foliations. Mesoperthitic intergrowth and well-developed allanite crystals suggest that they are deeply emplaced (Ricci 2006). Geochemical data point to an intermediate composition from monzogranite to granodiorite calcic-alkaline of medium-to-high K, sodic, metaluminous affinity, and enrichment in LILE and light rare-earth elements (LREE). They are interpreted as orogenic bodies emplaced at the climax of the continental collision of the Transamazonian cycle (Macambira and Ricci 2013). In the central portion of the BJD, charnockites analyzed by U-Pb SHRIMP and Pb-evaporation methods yielded zircon ages between 2114 and 2094 Ma (Faraco *et al.*

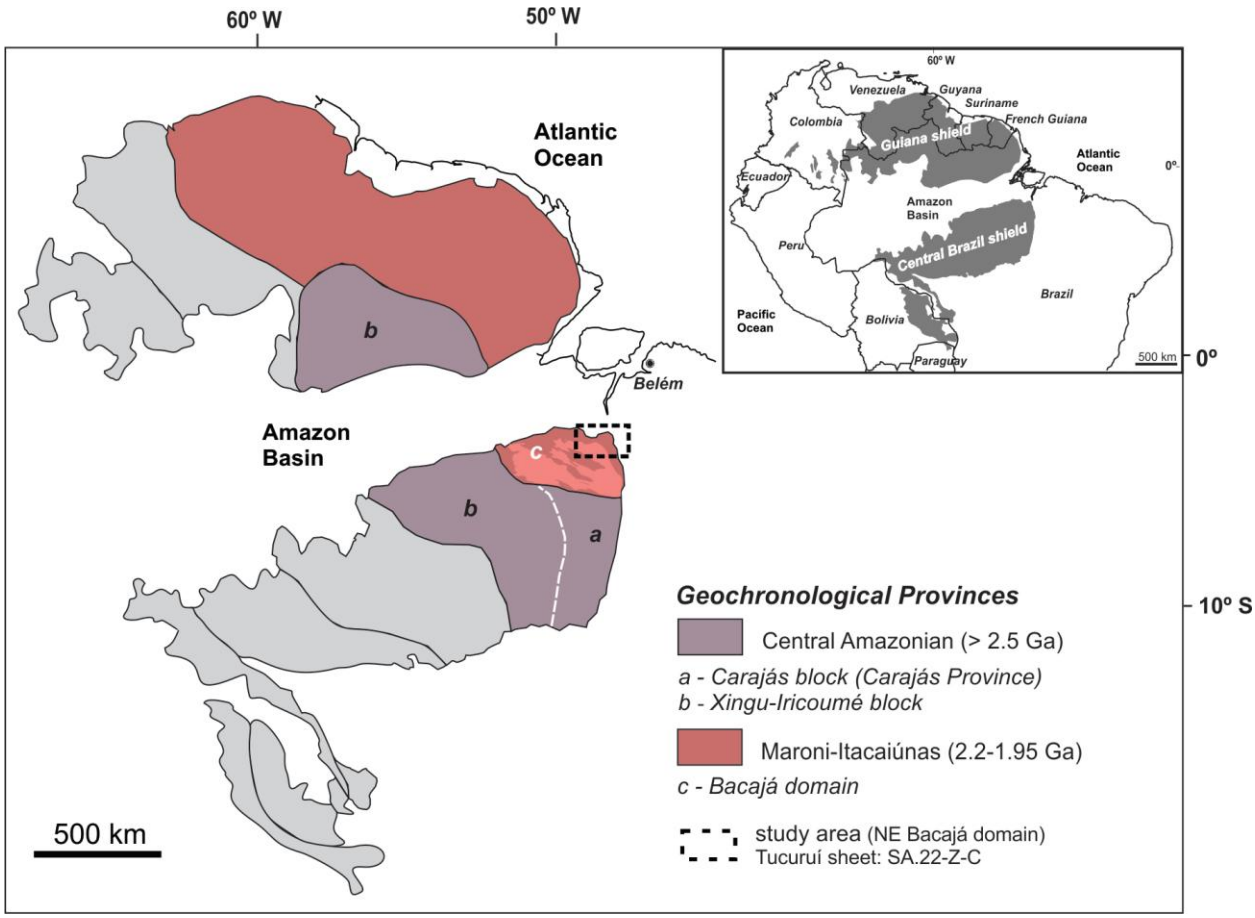

Figure 1. Sketch map of geochronological provinces from the Amazonian craton, based on Tassinari and Macambira (2004), with location of the tectonic domains of Vasquez *et al.* (2008b). Detail of the study area is shown in Fig. 2.

Table 1. Geochronological data from igneous and meta-igneous zircons of the northeastern and central portions of the Bacajá domain.

Rock	Unit	Area	Age (Ma)[a]	Method	Ref
Archaean					
Tonalitic gneiss		Manelão mine	2671 ± 3	Pb-Evaporation	2
Orthogneiss	Aruanã C.	Tucuruí sheet	2630 ± 15	U-Pb LA-ICPMS	1
Charnoenderbitic gneiss	Aruanã C.	Tucuruí sheet	2606 ± 4	Pb-Evaporation	3
Deformed Metamonzogranite	Aruanã C.	Bacajá River sheet	2586	Pb-Evaporation	4
Siderian					
2.44 Ga					
Quartz-dioritic gneiss		Brasil Novo	2440 ± 7	Pb-Evaporation	7
Quartz-monzodioritic gneiss		Belmonte village	2439 ± 4	Pb-Evaporation	2
2.4-2.3 Ga					
Metandesite	Três Palmeiras G.	Ressaca village	2417 ± 4	Pb-Evaporation	12
Metavolcanoclastic rock	Três Palmeiras G.	Ressaca village	2410 ± 7	Pb-Evaporation	12
Metandesite	Três Palmeiras G.	Zé Menezes mine	2359 ± 2	Pb-Evaporation	2
Metatonalite		Bacajá River	2338 ± 5	U-Pb SHRIMP	5
Tonalite		Novo Repartimento	2314 ± 9	U-Pb SHRIMP	8
Rhyacian					
2.2-2.18 Ga					
Granodiorite		Brasil Novo	2215 ± 2	Pb-Evaporation	7
Monzogranite		Belmonte village	2191 ± 2	Pb-Evaporation	2
Tonalite		Brasil Novo	2182 ± 6	U-Pb SHRIMP	9
2.16-2.10 Ga					
Monzodiorite		Galo Mine	2160 ± 3	U-Pb SHRIMP	5
Leucogranodiorite		Belo Monte	2154 ± 4	Pb-Evaporation	2
Tonalite		Xingu River	2133 ± 10/2340	U-Pb SHRIMP	5
Granitic mobilized		Tucuruí sheet	2122 ± 18 (M)	U-Pb LA-ICPMS	6
Orthogranulite		Tucuruí sheet	2120 ± 4	U-Pb LA-ICPMS	1
Granodiorite		Novo Repartimento	2114 + 35/-33	U-Pb SHRIMP	8
Metatonalite	Bacajaí C.	Tucuruí sheet	2103 ± 21	U-Pb LA-ICPMS	1
Pelitic paragneisses and migmatites		Xingu River	2109 ± 9 (M)	U-Pb SHRIMP	13
2.09-2.06 Ga					
Monzogranite	Bacajaí C.	Tucuruí sheet	2094 ± 11	U-Pb LA-ICPMS	1
Enderbite	Bacajaí C.	Tucuruí sheet	2090 ± 6	Pb-Evaporation	6
Monzogranite		Belo Monte	2086 ± 6	U-Pb SHRIMP	9
Orthogranulite		Tucuruí sheet	2086 ± 4	U-Pb LA-ICPMS	1
Felício Turvo Granite		Manelão mine	2085 ± 4	Pb-Evaporation	2
Syenogranite	Arapari I.S.	Tucuruí sheet	2080 ± 16	U-Pb LA-ICPMS	1
Granite	João Jorge I.S.	Tucuruí sheet	2077 ± 5	Pb-Evaporation	6
Leucogranodiorite		Novo Repartimento	2077 ± 3	Pb-Evaporation	2
Monzogranite		Xingu River	2077 ± 2	Pb-Evaporation	7
Granodiorite		Novo Repartimento	2076 ± 6/2110 ± 11	Pb-Evaporation	10
Pelitic paragneisses and migmatites		Xingu River	2071 ± 3/ 2057 ± 3[b] (M)	U-Pb SHRIMP	13
Felício Turvo Granite		Manelão Mine	2069 ± 6	Pb-Evaporation	11
Granodiorite	João Jorge I. S.	Tucuruí sheet	2062 ± 22	U-Pb LA-ICPMS	1
Charnockite	Arapari I. S.	Tucuruí sheet	2059 ± 4	Pb-Evaporation	6

1: This work; 2: Macambira *et al.* (2009); 3: Vasquez *et al.* (2008b); 4: Besser (2012); 5: Vasquez *et al.* (2008a); 6: Macambira and Ricci (2013); 7: Vasquez *et al.* (2005); 8: Faraco *et al.* (2005); 9: Santos (2003); Barros *et al.* (2007); 11: Souza *et al.* (2003); 12: Cristo (2018); 13: Vasquez *et al.* (2014); [a]magmatic ages obtained in zircon. Some are interpreted as metamorphic events (M); [b]age obtained in monazite.

2005, Monteiro 2006). Macambira and Ricci (2013) obtained a mean age of 2090 ± 6 Ma (Pb-evaporation in zircon), interpreted as being the crystallization age of this suite.

The Arapari Intrusive Suite is composed of charnockites, charno-enderbites, and granitoids with NW-SE foliations (Fig. 2). Macambira and Ricci (2013) described a texture variation from porphyritic to equigranular, banded to preserved rocks, deeply emplaced in similar conditions as the Bacajaí Complex. Those authors confirmed a crustal contribution on an active continental margin observed by a calcic-alkaline magmatism enriched in LILE and LREE. Pb-evaporation in zircon yielded crystallization ages of 2088 ± 2 Ma, 2069 ± 2 Ma, and 2059 ± 4 Ma. Macambira and Ricci (2013) suggested an interpretation that this unit was formed by several magmatic pulses. To the west, Pb-evaporation and U-Pb ages in zircon show values between 2086 and 2070 Ma (Santos 2003, Vasquez *et al.* 2008a, Macambira *et al.* 2009), Nd-T_{DM} ages of about 2.47 Ga and $\varepsilon Nd_{(t)}$ between -2.40 and -3.12 (Vasquez 2006).

The João Jorge intrusive suite is the youngest lithostratigraphic unit. It mainly consists of monzogranites and syenogranites that occur as NW-SE batholiths and stocks. Geochemical data show enrichment in LILE/LREE and depletion in HFSE and high rare-earth elements. They have affinity with post-collisional granites and preserved signature of volcanic arcs (Macambira and Ricci 2013). Pb-evaporation on the zircon method yielded ages of ca. 2.08 Ma (Vasquez *et al.* 2005, Macambira *et al.* 2009, Macambira and Ricci 2013). In the western portion of the BJD, Macambira *et al.* (2009) identified juvenile Siderian components ($\varepsilon Nd_{(2.08Ga)}$ = -0.6 and Nd-T_{DM} = 2.33 Ga) and some Neoarchaean crustal components ($\varepsilon Nd_{(2.08Ga)}$ = -4.12 and Nd-T_{DM} = 2.57 Ga).

ANALYTICAL METHODS

Zircon preparation and SEM images

After fieldwork (Macambira and Ricci 2013), zircon crystals were first concentrated by traditional conventional methods (crushing/grinding, granulometric, magnetic, and water/alcohol concentrations). Then, scanning electron microscopy (Zeiss SEM LS15 Scanning Electron Microscope) was performed at the laboratory of the CPRM, Belém (LAMIN-BE), using high vacuum (3.0–1.5 x 10^{-5} mPa) and tungsten filament mode with an EVO15RHS CL detector set at 13–14 kV, 10 Na input current. Cathodoluminescence (CL) images of zircon crystals were obtained using a LEO-ZEISS 1430 scanning electron microscope in the Microanalysis Laboratory (LabMev) at Universidade Federal do Pará (UFPA), Belém. All zircons are within the fraction 175-125 µm, and the images were used for choosing the most suitable sites for analysis, avoiding inclusions, and keeping away from metamict and highly fractured sites.

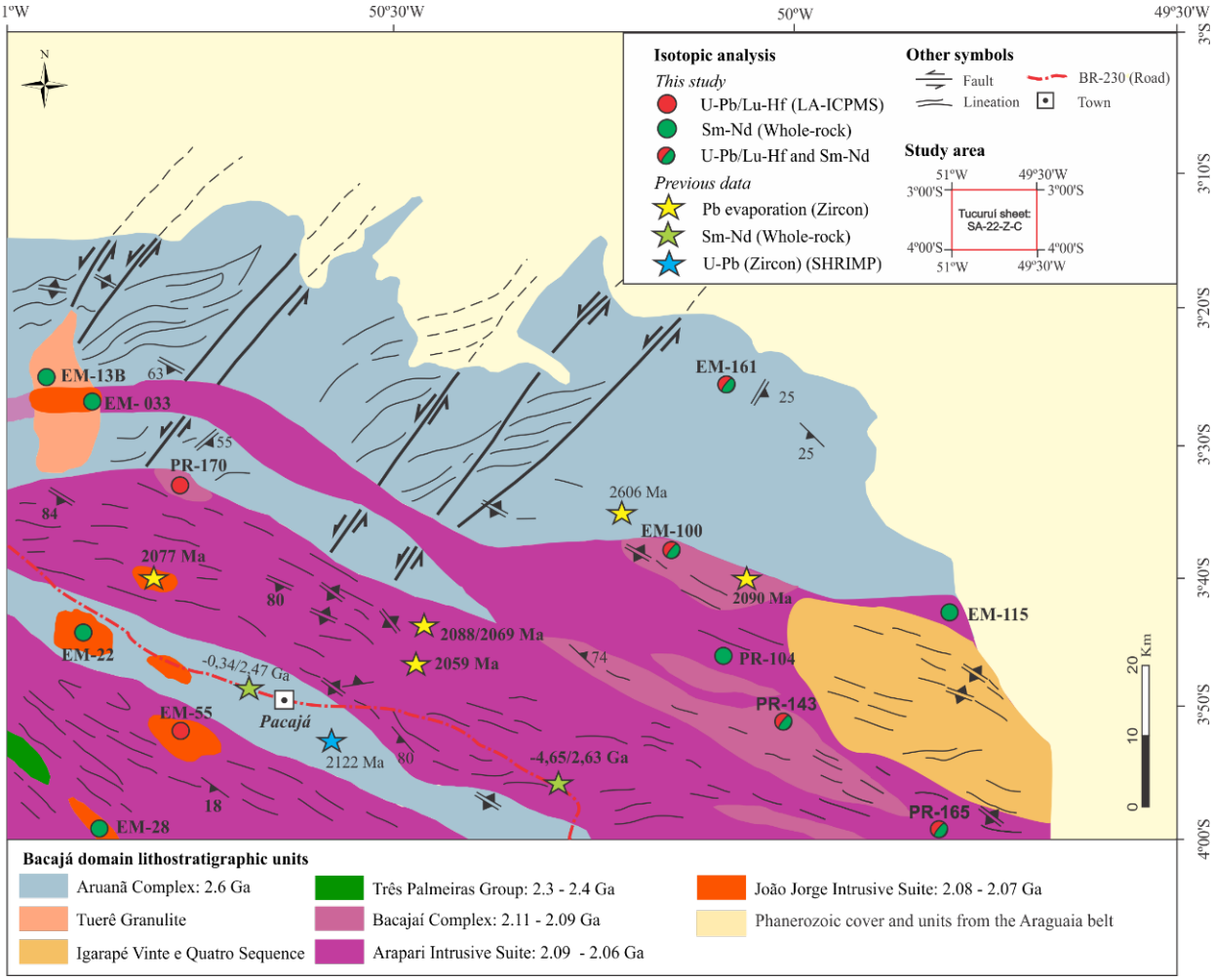

Figure 2. Geological map of the NE Bacajá domain: Tucuruí sheet SA.22-Z-C (modified from Macambira and Ricci 2013, CPRM 2016). Previous data: Pb-evaporation and U-Pb SHRIMP in zircon (Vasquez *et al.* 2008b, Macambira and Ricci 2013); Sm-Nd on whole rock (Macambira *et al.* 2009).

Zircon U-Pb dating

LA-ICP-MS U-Pb isotopic analyses were carried out using a multi-collector Neptune Thermo Finnigan mass spectrometer coupled with a Nd:YAG LSX-213 G2 CETAC laser microprobe in the Isotopic Geology Laboratory (Pará-Iso) at UFPA. The analytical sequence alternates sample collection with GJ-1 reference zircon (608 ± 1.5 Ma; Jackson *et al.* 2004) for fractionation and correction of mass discrimination. The Plesovice (337 Ma; Slama *et al.* 2008) standard zircon was also used as secondary reference material and obtained the weighted mean $^{206}Pb/^{238}U$ age of 340.4 ± 3.6 Ma (n = 11, MSWD = 0.063). Isotopic ratios ($^{206}Pb/^{238}U$, $^{207}Pb/^{235}U$, and $^{207}Pb/^{206}Pb$) and ages were calculated from the background-corrected values and ^{204}Hg interference over ^{204}Pb. For the correction of common lead contribution, the terrestrial Pb evolution model over time of Stacey and Kramers (1975) has been used. Instrumental parameters, spectrometer, and laser settings are all in accordance with the parameters set by Milhomem Neto and Lafon (2019), in addition to the protocols for correcting isotopic ratios ($^{206}Pb/^{238}U$, $^{232}Th/^{238}U$, $^{207}Pb/^{206}Pb$) and reductions of raw data processed in Excel spreadsheets (ISOPLOT/EX 3.0 by Ludwig 2003) for age calculation.

Zircon Lu-Hf

The procedure of in situ Lu-Hf zircon analyses was carried out in the same equipment for the U-Pb analysis at Pará-Iso (UFPA). Analytical sequence alternates sample crystals with reference crystals with known values for the determined $^{176}Hf/^{177}Hf$ ratios of GJ-1 (0.282025 ± 0.000185; 2σ; n = 12). Normalization procedures are according to Thirlwall and Anczkiewicz (2004) for isotopic ratios of Yb ($^{173}Yb/^{171}Yb$ = 1.12346), Patchett and Tatsumoto (1980) for Hf isotopic rations ($^{179}Hf/^{177}Hf$ = 0.7325), and Chu *et al.* (2002) with Thirlwall and Anczkiewicz (2004) for the correction of isobaric interferences of ^{176}Lu and ^{176}Yb ($^{176}Lu/^{175}Lu$ = 0.026549; $^{176}Yb/^{173}Yb$ = 0.786956; respectively).

The raw data file from the mass spectrometer was retrieved into an Excel spreadsheet for processing in order to calculate the corrected isotopic ratios for each point (blank analysis was also taken into account). The standard procedure cycle consists of the analysis of blank, GJ-1, MudTank, sample (at least 10 zircon crystals), and finishes with the same initial sequence that begins a new cycle for another sample. Calculations of εHf used a decay constant of 1.867 × 10^{-11} $years^{-1}$ (Scherer *et al.* 2001, Soderlund *et al.* 2004), present-day ratio of $^{176}Lu/^{177}Hf$ of 0.0336, and a ratio of $^{176}Hf/^{177}Hf$ of 0.282785 for the chondritic uniform reservoir (CHUR) (Bouvier *et al.* 2008). The $^{176}Lu/^{177}Hf$ of 0.0388 and $^{176}Hf/^{177}Hf$ of 0.28325 were used for depleted mantle (DM) (Andersen *et al.* 2009), and for crustal model ages (T_{DM}^{C}), a $^{176}Lu/^{177}Hf$ of 0.015 was assumed as a continental crust average value (Griffin *et al.* 2004). As for the U-Pb analysis, instrumental parameters, spectrometer, and laser settings are all also in accordance with the parameters set by Milhomem Neto and Lafon (2019), who established a routine in this laboratory for those methods.

Sm-Nd whole rock

For the Sm-Nd analyses, approximately 100 mg of rock powder were dissolved with a mixture of HF and HNO_3 and a mixed ^{150}Nd-^{149}Sm spike. REE were separated by cation exchange chromatography (Dowex 50WX-8 resin) using HCl and HNO_3. Then, Sm and Nd were separated from the other REE by anion exchange chromatography (Dowex AG1-X4 resin) using a mixture of HNO_3 and methanol. Isotopic ratios were measured on a Finnigan MAT 262 thermo-ionization mass spectrometer. Nd is normalized to a $^{146}Nd/^{144}Nd$ ratio of 0.7219. Total procedural blanks during the analysis were lower than 0.1%, and values obtained for the La Jolla and BCR-1 reference materials were in agreement with the literature. The decay constant used was 6.54 × 10^{-12} $years^{-1}$ and the chondritic values used to calculate εNd were $^{143}Nd/^{144}Nd$ = 0.512638 and $^{147}Sm/^{144}Nd$ = 0.1967. The crustal residence ages were calculated using DePaolo's (1988) model for DM.

RESULTS

U-Pb and Lu-Hf in zircon

Zircon crystals from six samples from the northeastern region of the BJD were dated. Among the results, listed in Table 1 and represented in the concordia diagrams, the red ellipses were not used in the elaboration of the discordia line to obtain the age of the upper intercept. Discordant points in the concordia diagram or, less frequently, those that diverged from the average age were discarded. Coherent concordant U-Pb ages or, in most cases, the age of the upper intercept of each sample were used to calculate the Lu-Hf parameters. Spots of 50 μm for the analyses of Lu-Hf were targeted at or near the U-Pb analytical point.

Orthogneiss EM-161A (Aruanã Complex)

Sample EM-161A shows a medium- to coarse-grained porphyroclastic texture, strongly banded with an augen structure. The megacrystals (> 1 cm) of microcline (40%) are mantled by a lepidoblastic biotite (10%) and the granoblastic matrix comprises quartz, plagioclase, K-feldspar with polygonal contacts, and titanite (5%) (Fig. 3A). Myrmekite intergrowth is common. Accessory minerals include zircon, apatite, clinopyroxene, and a secondary assemblage is constituted of epidote, opaques, and chlorite.

The zircon crystals are brown in color and elongated, prismatic, and euhedral to subhedral in shape. CL images show fading patchy zoning (Fig. 4D1) and luminescent apatite inclusions (Fig. 4D3). The U-Pb analyses were performed on 20 crystals, 6 of which were used to obtain a discordia, whose upper intercept yielded the crystallization age of the igneous protolith of 2630 ± 15 Ma (MSWD = 0.44, Fig. 5A). Nine concordant to subconcordant zircon crystals yielded negative values from -0.3 to -1.7 of $εHf_{(2.63\ Ga)}$ and Hf-T_{DM}^{C} model age range between 3.2 and 3.1 Ga (Table 2).

Orthogranulite PR-143

Sample PR-143 shows a medium-grained granoblastic texture, polysynthetic deformation twins in plagioclase, equigranular augite crystals, and myrmekite intergrowth. Plagioclase (50%) and quartz (10%) are the main felsic minerals affected by strong deformation and recrystallization. Pyroxenes (15%) vary from prismatic, elongated, and locally oriented, just as biotite (25%) varies from orthopyroxene to equigranular polygonal aggregates of augite. The most abundant accessory minerals are zircon and opaques.

Zircon crystals are mainly subhedral. CL images show convoluted zoning (Fig. 6A4), weak or no internal zoning (Fig. 6C9), and rims of the grains with greater luminescence that surround all crystals (Fig. 6C9). A total of 23 crystals were analyzed using the U-Pb method, and it was possible to individualize two different concordant ages. The lower age was 2086 ± 4 Ma (MSDW < 1, n = 4), while the higher age was 2120 ± 4 Ma (MSDW < 1, n = 6), without overlapping (taking the errors into account) (Fig. 5B). These two different ages obtained in the U-Pb analyses are supported by the Lu-Hf results. Seven U-Pb concordant and three subconcordant crystals from this sample were analyzed by this method. The younger group yielded exclusively negative values for $\varepsilon Hf_{(t = 2.09\ Ga)}$, ranging between -1.2 and -3.2, whereas the older group yielded mainly positive values, and some slightly negative values for $\varepsilon Hf_{(t = 2.12\ Ga)}$, ranging from 2.5 to -0.8. The Hf-T_{DM}^{C} model ages are also different, 2.9–2.7 Ga and 2.7–2.5 Ga for the youngest and oldest groups, respectively (Table 2).

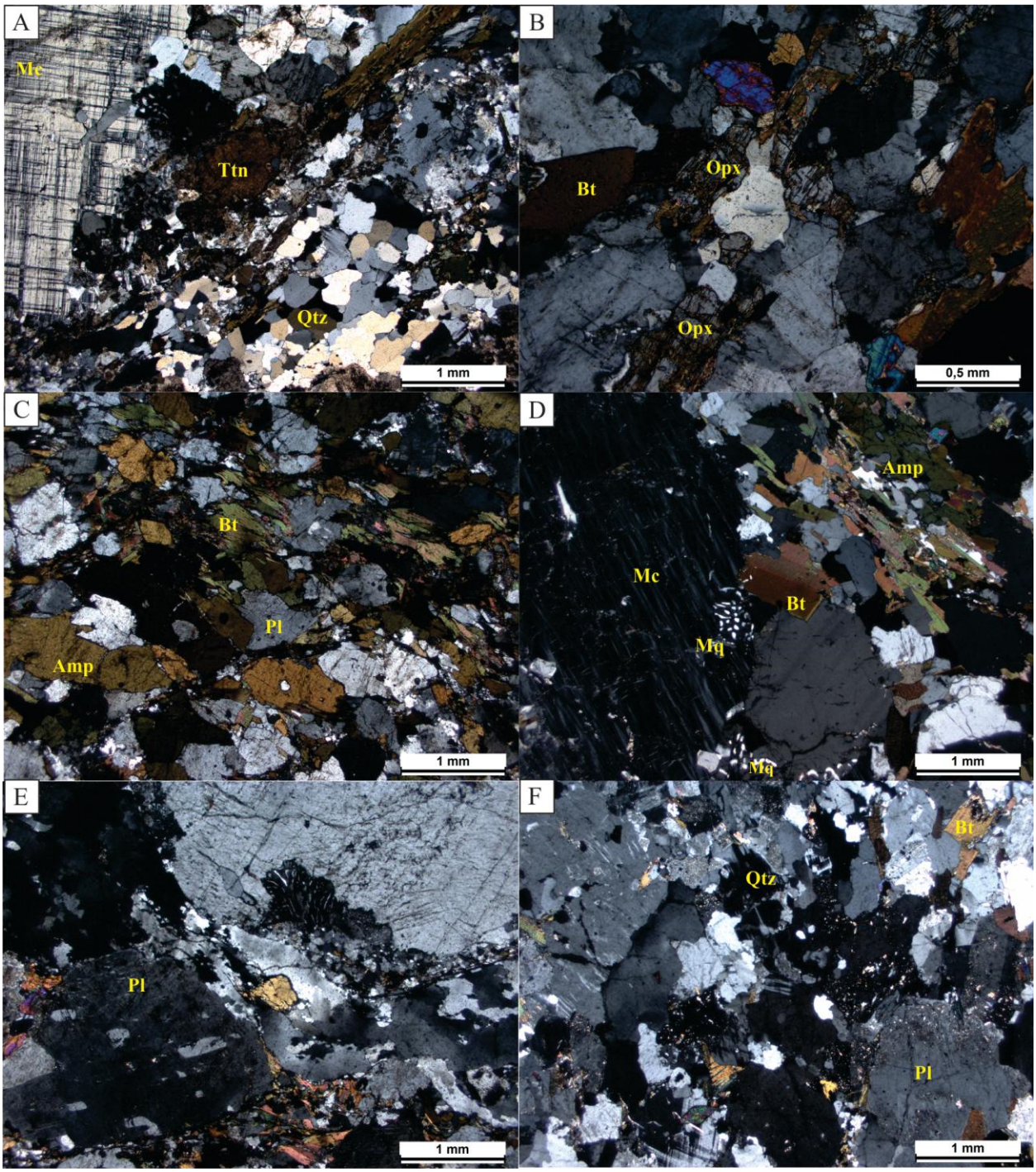

Mc: microcline; Ttn: titanite; Qtz: quartz; Bt: biotite; Opx: orthopyroxene; Cpx: Clinopyroxene; Mq: Myrmekite; Amp: Amphibole; Pl: Plagioclase.

Figure 3. Thin section microphotographs of representative petrographic features of the rocks studied. (A) Orthogneiss EM-161A. (B) Orthogranulite PR-143. (C) Metatonalite EM-100. (D) Monzogranite PR-170. (E) Syenogranite PR-165. (F) Granodiorite EM-55.

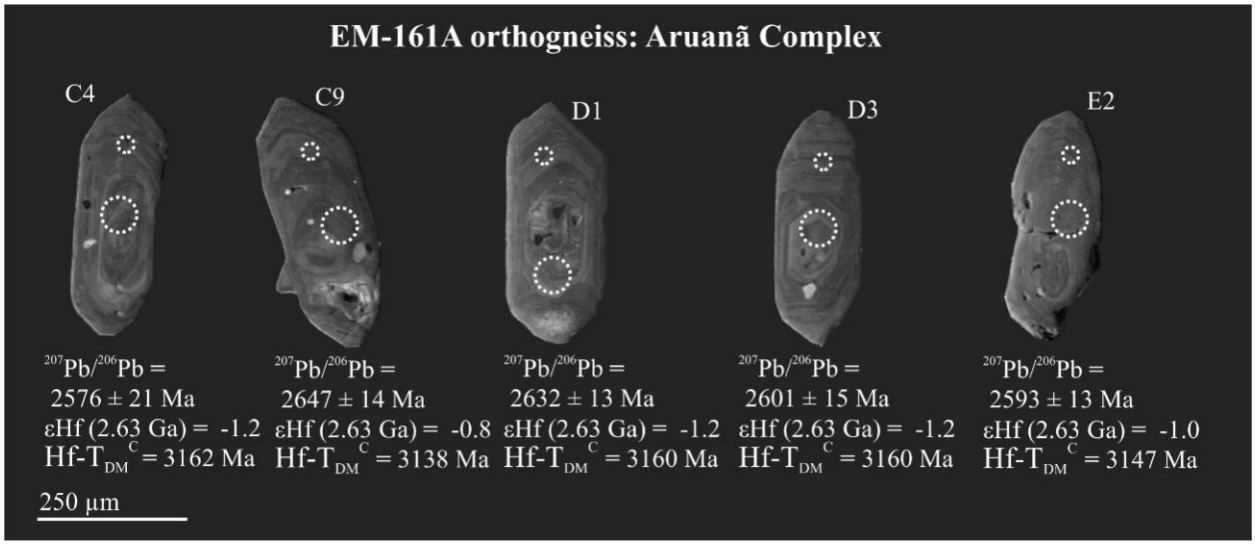

Figure 4. CL images of representative EM-161A zircon grains. Circles indicate spot locations, with the small ones being U-Pb and the large ones being Lu-Hf.

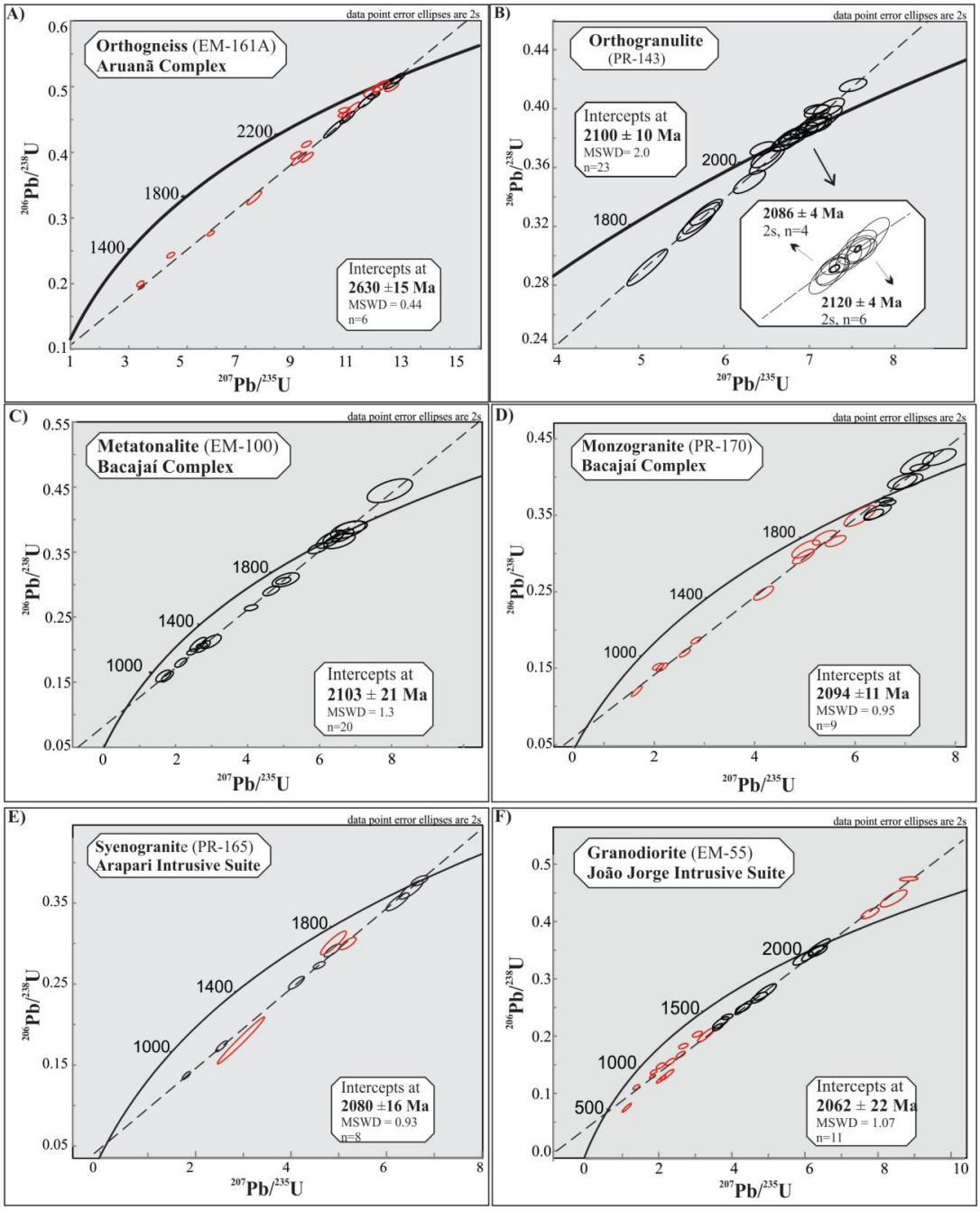

Figure 5. Concordia diagrams for zircon U-Pb results. Red ellipses were disregarded for the age calculation.

Table 2. Lu-Hf isotopic data on zircon from the NE Bacajá domain.

ID	$^{176}Hf/^{177}Hf$	2σ	$^{176}Lu/^{177}Hf$	2σ	$^{176}Yb/^{177}Hf$	2σ	$^{178}Hf/^{177}Hf$	2σ	εHf (0)	t (U-Pb)	$(^{176}Hf/^{177}Hf)_t$	εHf(t)	T_{DM}	T_{DM}^C
EM-161A orthogneiss: Aruanã Complex														
C4	0.281090	0.000045	0.000603	0.000024	0.040459	0.001514	1.467278	0.000039	-59.94	2,630	0.281060	-1.2	2947	3162
C9	0.281098	0.000057	0.000553	0.000048	0.035287	0.002762	1.467267	0.000052	-59.65	2,630	0.281070	-0.8	2932	3138
D1	0.281095	0.000035	0.000680	0.000014	0.046017	0.000587	1.467261	0.000044	-59.77	2,630	0.281061	-1.2	2946	3160
D3	0.281084	0.000040	0.000459	0.000033	0.029893	0.002378	1.467260	0.000041	-60.17	2,630	0.281060	-1.2	2944	3160
E2	0.281098	0.000050	0.000622	0.000043	0.045571	0.001025	1.467187	0.000087	-59.67	2,630	0.281066	-1.0	2938	3147
E5	0.281109	0.000047	0.000473	0.000007	0.032413	0.000541	1.467247	0.000037	-59.26	2,630	0.281085	-0.3	2911	3105
F8	0.281114	0.000033	0.000611	0.000027	0.039553	0.000972	1.467262	0.000053	-59.10	2,630	0.281083	-0.4	2915	3110
G3	0.281081	0.000040	0.000656	0.000018	0.042551	0.000739	1.467215	0.000036	-60.25	2,630	0.281048	-1.6	2962	3188
H6	0.281070	0.000047	0.000463	0.000047	0.032690	0.002738	1.467135	0.000083	-60.64	2,630	0.281047	-1.7	2962	3191
PR-143 orthogranulite														
A5	0.281437	0.000040	0.000596	0.000027	0.043150	0.002332	1.467274	0.000050	-47.68	2,120	0.281413	-0.6	2484	2726
B2	0.281456	0.000032	0.000477	0.000025	0.032697	0.001816	1.467278	0.000037	-47.00	2,120	0.281437	0.3	2451	2673
C2	0.281429	0.000047	0.000570	0.000022	0.043433	0.002448	1.467214	0.000049	-47.97	2,120	0.281406	-0.8	2493	2742
C4	0.281405	0.000050	0.000194	0.000007	0.013888	0.000569	1.467220	0.000049	-48.81	2,086	0.281397	-1.9	2501	2784
C9	0.281485	0.000048	0.000688	0.000049	0.049581	0.003000	1.467265	0.000062	-45.97	2,120	0.281457	1.0	2425	2627
D2	0.281442	0.000052	0.000644	0.000047	0.047827	0.002387	1.467259	0.000054	-47.50	2,086	0.281416	-1.2	2480	2741
D3	0.281525	0.000046	0.000695	0.000042	0.048328	0.002748	1.467237	0.000052	-44.54	2,120	0.281497	2.5	2371	2537
D4	0.281390	0.000048	0.000712	0.000053	0.051475	0.001978	1.467281	0.000051	-49.34	2,086	0.281362	-3.2	2554	2863
D8	0.281418	0.000027	0.000156	0.000006	0.010362	0.000379	1.467265	0.000046	-48.35	2,086	0.281411	-1.4	2481	2752
A4	0.281460	0.000041	0.000515	0.000054	0.036438	0.002114	1.467292	0.000059	-46.87	2,120	0.281439	0.4	2668	2668
EM-100 metatonalite: Bacajaí Complex														
A4	0.281466	0.000043	0.000992	0.000084	0.062984	0.003299	1.467269	0.000052	-46.64	2,100	0.281426	-0.5	2469	2709
B2	0.281421	0.000041	0.000887	0.000023	0.054282	0.000659	1.467312	0.000036	-48.22	2,100	0.281386	-2.0	2523	2799
B3	0.281493	0.000040	0.001306	0.000064	0.079362	0.003661	1.467246	0.000049	-45.70	2,100	0.281440	0.0	2453	2678
C1	0.281426	0.000039	0.000913	0.000015	0.055953	0.001273	1.467290	0.000051	-48.05	2,100	0.281390	-1.8	2518	2790
C2	0.281466	0.000050	0.001110	0.000045	0.068025	0.001716	1.467277	0.000036	-46.64	2,100	0.281422	-0.7	2477	2719
C4	0.281465	0.000045	0.001141	0.000017	0.068298	0.001799	1.467245	0.000045	-46.69	2,100	0.281419	-0.8	2481	2725
D1	0.281452	0.000042	0.000933	0.000015	0.057726	0.001326	1.467169	0.000077	-47.12	2,100	0.281415	-0.9	2484	2734
G1	0.281422	0.000055	0.001046	0.000094	0.063635	0.001805	1.467272	0.000056	-48.22	2,100	0.281380	-2.2	2533	2813
H1	0.281511	0.000038	0.000986	0.000103	0.060753	0.003800	1.467242	0.000039	-45.06	2,100	0.281471	1.1	2409	2609
I3	0.281458	0.000047	0.001139	0.000019	0.070637	0.001496	1.467213	0.000056	-46.93	2,100	0.281412	-1.0	2490	2740
A1	0.281512	0.000043	0.000682	0.000047	0.039093	0.002008	1.467260	0.000058	-45.01	2,100	0.281485	1.5	2388	2579
PR-170 monzogranite: Bacajaí Complex														
A2	0.281508	0.000031	0.000756	0.000098	0.044049	0.003364	1.467250	0.000039	-45.15	2,094	0.281478	1.2	2398	2598
B1	0.281528	0.000036	0.000903	0.000037	0.058774	0.001620	1.467220	0.000039	-44.43	2,094	0.281492	1.7	2380	2566
B3	0.281511	0.000041	0.000656	0.000050	0.041587	0.002731	1.467219	0.000045	-45.05	2,094	0.281485	1.4	2388	2583
C5	0.281518	0.000032	0.000975	0.000058	0.054860	0.003128	1.467231	0.000034	-44.79	2,094	0.281479	1.2	2398	2595
D2	0.281514	0.000034	0.001396	0.000124	0.075024	0.003670	1.467236	0.000033	-44.95	2,094	0.281458	0.5	2430	2643
E5	0.281466	0.000037	0.001427	0.000158	0.064882	0.005212	1.467241	0.000051	-46.66	2,094	0.281409	-1.3	2498	2753
H5	0.281476	0.000031	0.001075	0.000092	0.043383	0.003186	1.467254	0.000037	-46.27	2,094	0.281434	-0.4	2461	2697
H9	0.281488	0.000061	0.000484	0.000013	0.034210	0.000650	1.467256	0.000052	-45.87	2,094	0.281469	0.8	2408	2619
I2	0.281449	0.000050	0.000520	0.000041	0.034605	0.001577	1.467242	0.000049	-47.24	2,094	0.281429	-0.6	2462	2708
I4	0.281504	0.000048	0.000563	0.000038	0.036359	0.001712	1.467274	0.000044	-45.30	2,094	0.281481	1.3	2392	2590
PR-165 syenogranite: Arapari Intrusive Suite														
B6	0.281483	0.000041	0.000766	0.000047	0.052683	0.003235	1.467218	0.000048	-46.05	2,080	0.281453	-0.1	2432	2664
C2	0.281435	0.000042	0.000556	0.000048	0.036401	0.000974	1.467241	0.000055	-47.73	2,080	0.281413	-1.5	2483	2752
C4	0.281499	0.000043	0.000878	0.000051	0.054667	0.002751	1.467228	0.000055	-45.47	2,080	0.281464	0.4	2418	2638
D9	0.281485	0.000045	0.000633	0.000034	0.037971	0.001925	1.467235	0.000034	-45.97	2,080	0.281460	0.2	2421	2648
E8	0.281499	0.000039	0.000359	0.000024	0.024626	0.001239	1.467254	0.000047	-45.48	2,080	0.281485	1.1	2386	2592
G3	0.281473	0.000037	0.000806	0.000049	0.055234	0.001981	1.467257	0.000047	-46.39	2,080	0.281441	-0.5	2448	2690
G5	0.281457	0.000039	0.000496	0.000024	0.025560	0.001319	1.467250	0.000038	-46.94	2,080	0.281438	-0.6	2450	2697
G10	0.281437	0.000042	0.000574	0.000029	0.037297	0.001426	1.467225	0.000040	-47.68	2,080	0.281414	-1.4	2482	2750
I3	0.281392	0.000037	0.000484	0.000010	0.035752	0.000974	1.467237	0.000052	-49.25	2,080	0.281373	-2.9	2536	2841
EM-55 granodiorite: João Jorge Intrusive Suite														
A3	0.281506	0.000038	0.000606	0.000087	0.035289	0.003596	1.467255	0.000036	-45.22	2,060	0.281483	0.5	2391	2611
D9	0.281523	0.000051	0.000328	0.000010	0.021972	0.000669	1.467255	0.000056	-44.61	2,060	0.281511	1.5	2351	2549
E2	0.281527	0.000035	0.001075	0.000059	0.077914	0.002775	1.467286	0.000034	-44.50	2,060	0.281485	0.6	2392	2607
E5	0.281481	0.000039	0.000546	0.000013	0.039834	0.000820	1.467232	0.000038	-46.10	2,060	0.281460	-0.3	2421	2662
E7	0.281538	0.000041	0.000542	0.000044	0.040002	0.002878	1.467256	0.000059	-44.09	2,060	0.281517	1.8	2345	2534
F7	0.281527	0.000040	0.000556	0.000047	0.038303	0.001874	1.467254	0.000038	-44.48	2,060	0.281505	1.3	2360	2560
H6	0.281525	0.000044	0.000559	0.000025	0.040480	0.001261	1.467255	0.000055	-44.56	2,060	0.281503	1.3	2363	2565
I3	0.281518	0.000035	0.000750	0.000167	0.046403	0.007238	1.467252	0.000045	-44.79	2,060	0.281489	0.8	2384	2597
J1	0.281494	0.000058	0.000505	0.000062	0.032746	0.002770	1.467246	0.000044	-45.64	2,060	0.281474	0.2	2401	2629

For calculation: $\lambda = 1.867 \times 10^{-11}$ years^{-1} (Scherer *et al.* 2001, Soderlund *et al.* 2004); $^{176}Lu/^{177}Hf = 0.0336$ and $^{176}Hf/^{177}Hf = 0.282785$ for present day values of CHUR (Bouvier *et al.* 2008). $^{176}Lu/^{177}Hf = 0.0388$ and $^{176}Hf/^{177}Hf = 0.283225$ for the depleted mantle (DM) (Andersen *et al.* 2009). Single-stage model age (T_{DM}) using the measured $^{176}Lu/^{177}Hf$ and $^{176}Hf/^{177}Hf$. Two-stage crustal model age (T_{DM}^c) using the respective U-Pb age and $^{176}Lu/^{177}$ Hf = 0.015 for the average continental crust (Griffin *et al.* 2002, 2004). T (U-Pb), T_{DM} and T_{DM}^C are in Ma.

Metatonalite EM-100 (Bacajaí Complex)

Sample EM-100 exhibits banding with porphyroclastic texture, medium- to fine-grained, mostly inequigranular. Phenocrysts of plagioclase (35%) are mantled by strongly oriented hornblende (20%) and biotite (25%), present albite twinning, and vary from rounded to stubby crystals. Quartz (20%) is subhedral in the form of aggregates, has irregular contacts, and locally surrounds plagioclase crystals. Accessory phases are zircon and opaques, while epidote, chlorite, sericite, and clay minerals are alteration products.

Zircon crystals range from euhedral to subhedral, and elongated to prismatic in shape. There are many features of zoning loss (Figs. 7B2, 7B3, and 7C2) and metamictization (Figs. 7A1, 7A4, and 7C4). There is a distinct zone where luminescence is more intense at or around the rims. From the analyses of 20 zircon crystals, an age of 2103 ± 21 Ma (MSWD = 1.3, Fig. 5C) at the upper intercept was obtained. Ten zircon crystals were analyzed for Lu-Hf: two U-Pb concordant (99%), four subconcordant (98–95%), and five (< 95%) discordant. The values of $\varepsilon Hf_{(t = 2.1Ga)}$ are predominantly negative, ranging from 1.5 to -2.2, while the ages of model Hf-T_{DM}^{C} vary between 2.8 and 2.6 Ga (Table 2).

Monzogranite PR-170 (Bacajaí Complex)

Sample PR-170 exhibits a medium- to coarse-grained hypidiomorphic to porphyroclastic texture. Tabular, poikilitic, and subhedral phenocrysts of alkali feldspar (microcline: 25%) are mantled by quartz (30%), plagioclase (25%), and hornblende (10%). It represents a typical granitic composition. The matrix is mainly granular, weakly deformed, and the overall texture preserves an igneous origin. Myrmekite and perthitic intergrowths are common, and a locally occurring quartz ribbon is identified. Accessory minerals are zircon, titanite, and opaques. Secondary assemblages are sericite (an alteration of feldspar) and biotite (an alteration of hornblende).

The zircon crystals are brown in color and prismatic, and euhedral to subhedral in shape. CL images show conspicuous oscillatory zoning (Fig. 8), and some crystals exhibit rims with a strong luminescence and more shaped (darker) areas. On the upper intercept, the most concordant crystals yielded a

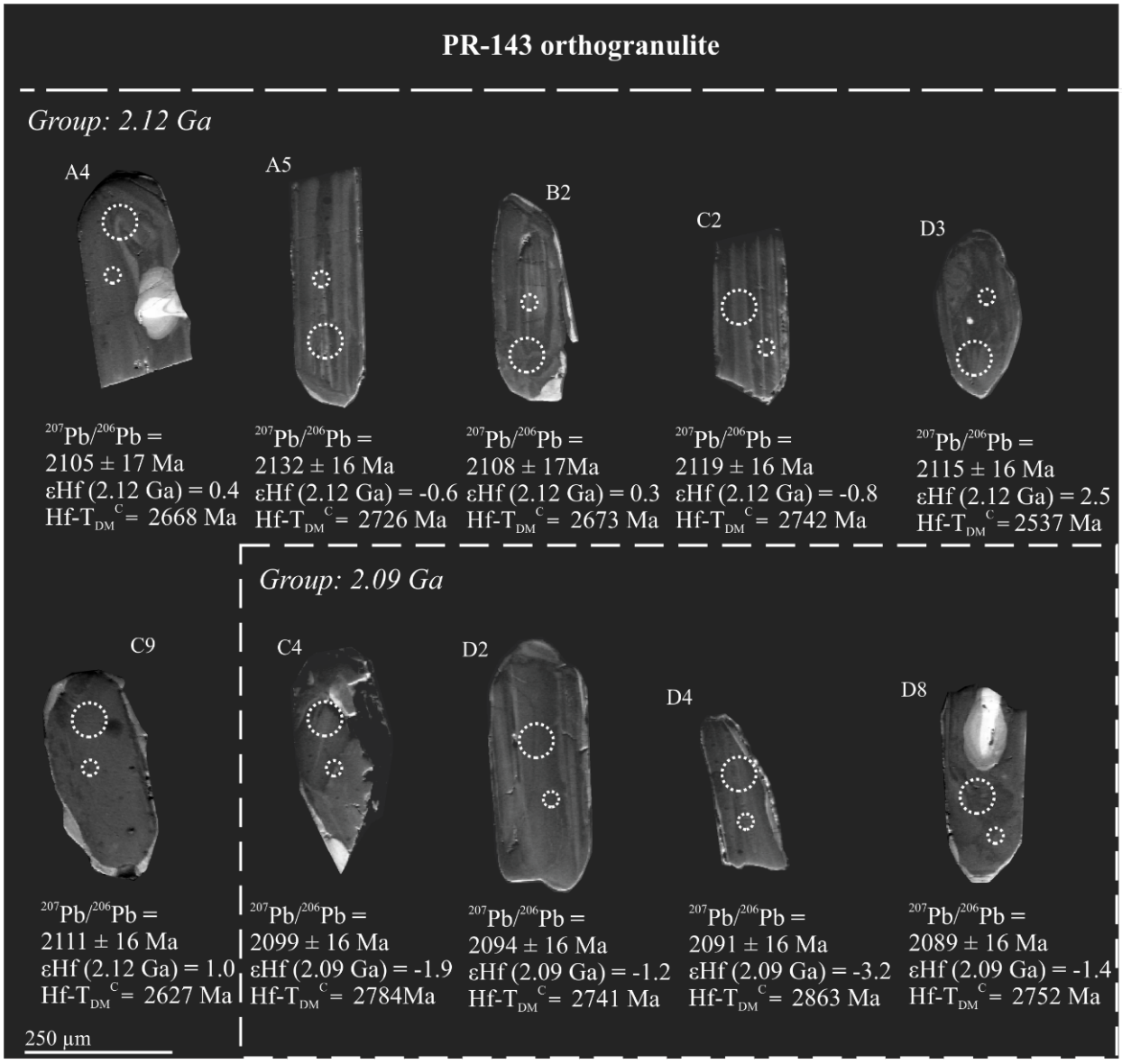

Figure 6. CL images of representative zircon grains of PR-143 orthogranulite. Circles indicate spot locations, with the small ones being U-Pb and the large ones being Lu-Hf.

crystallization age of 2094 ± 11 Ma (MSWD = 0.95, Fig. 5D). The $\varepsilon Hf_{(t=2.09\,Ga)}$ from 10 zircon crystals showed scattered results, ranging from positive to negative values of 1.7 to -1.3. The model Hf-T_{DM}^{C} age varied between 2.7 and 2.6 Ga (Table 2).

Syenogranite PR-165 (Arapari Intrusive Suite)

Sample PR-165 shows a porphyroclastic texture. Mortar texture, perthitic, antiperthitic, and myrmekite intergrowth are also quite common. Megacrystals (> 3 cm) are mainly of poikilitic microcline (60%) and subordinate plagioclase (10%). Quartz (25%) crystals are elongated and show a ribbon texture; locally, they are recrystallized and present a granoblastic texture. Igneous textures are partially preserved, such as the subhedral megacrystals (feldspar), which have been very little recrystallized or not at all. In addition, the typical Carlsbad twinning is well preserved and even observable with the naked eye. Mylonitization is more pronounced, and a protomylonitic foliation is identified, mainly by oriented biotite (5%). The matrix is comminuted but still keeps its preserved and rotated porphyroclasts (Fig. 3E). Accessory minerals are hornblende and zircon.

Zircon crystals from sample PR-165 are brown in color and subhedral in shape. CL images show well-developed oscillatory zoning, many inclusions, and low luminescence (Fig. 9). Most crystals from this sample show high values of common Pb, which were not considered in the calculation. However, an upper intercept was obtained with an age of 2080 ± 16 Ma (MSWD = 0.93, Fig. 5E) from eight analytical points ($f_{206} < 0.02$). Nine zircon crystals from this sample were subjected to analysis by the Lu-Hf method. The values of $\varepsilon Hf_{(t=2.08\,Ga)}$ vary between 1.1 and -2.9, and the Hf-T_{DM}^{C} model age varies between 2.8 and 2.6 Ga (Table 2).

Granodiorite EM-55 (João Jorge Intrusive Suite)

Sample EM-55 exhibits a medium-grained, hypidiomorphic texture (Fig. 3F). Cross-hatch twinning and perthitic

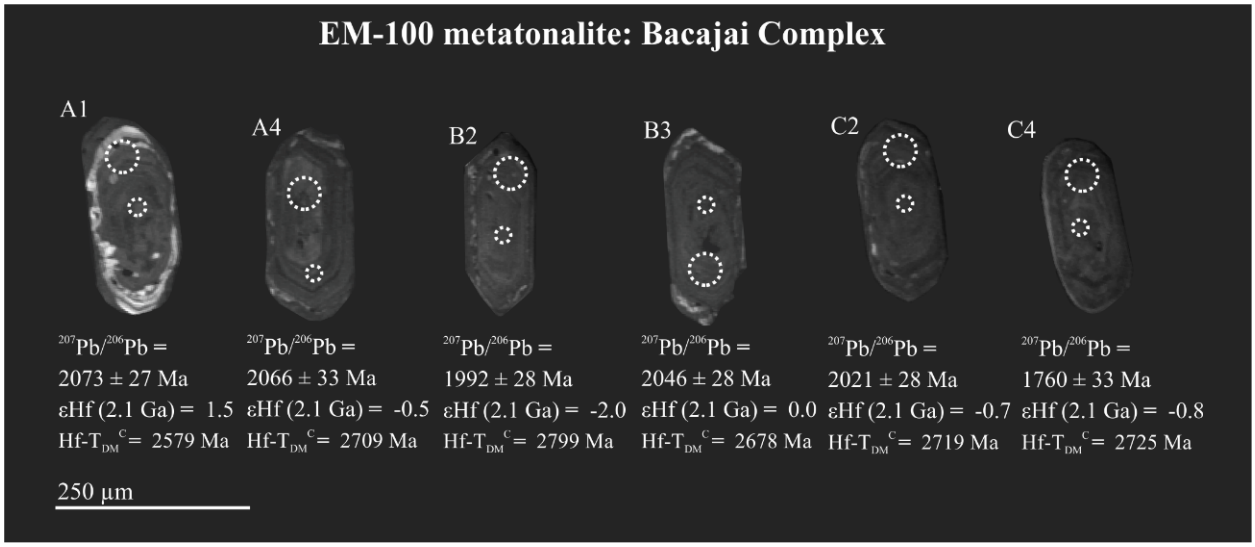

Figure 7. CL images of representative EM-100 metatonalite zircon grains from the Bacajaí Complex. Circles indicate spot locations, with the small ones being U-Pb and the large ones being Lu-Hf.

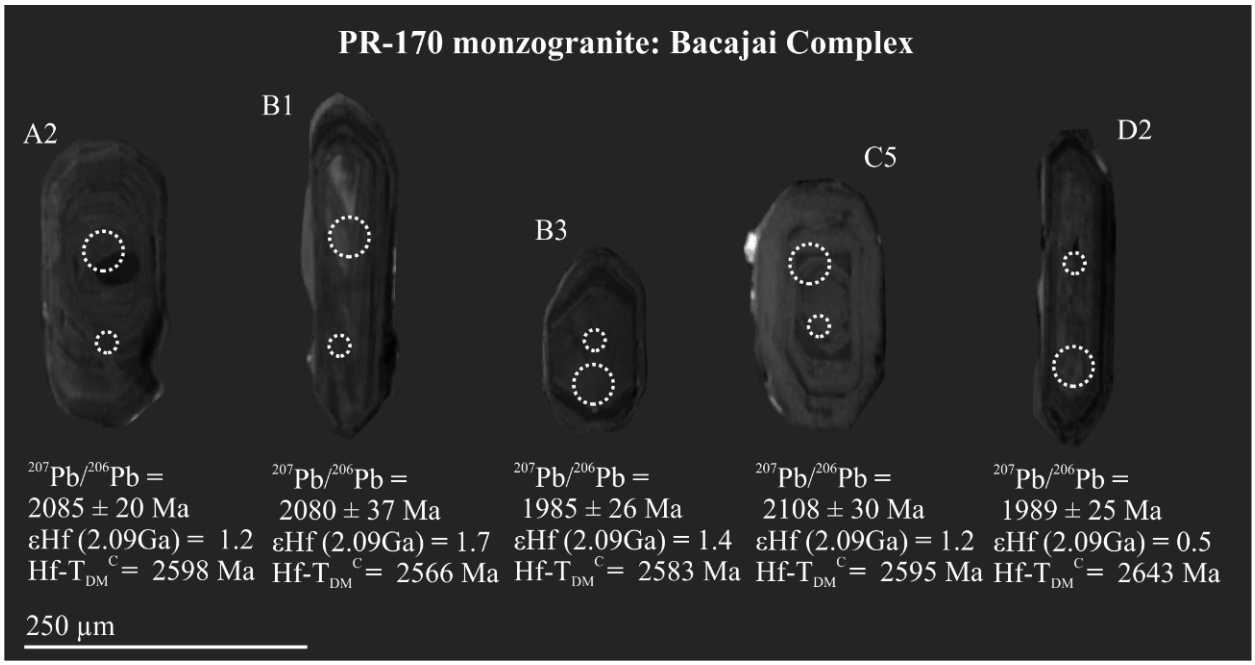

Figure 8. CL images of representative zircon grains from PR-170 monzogranite from the Bacajaí Complex. Circles indicate spot locations, with the small ones being U-Pb and the large ones being Lu-Hf.

intergrowth are diagnostic features for microcline crystals (20%). Plagioclase (40%) varies from crystals that show albite to absent twinning, locally myrmekite intergrowth, and sericite alteration are identified. Quartz (35%) is recrystallized and exhibits undulose extinction, ribbon quartz types, and polygonal mosaic. Biotite (5%) is strongly oriented with variations to the mica fish microtexture. Accessory minerals are prismatic titanite and zircon. The secondary phase is mainly sericite.

Zircon populations are brown in color, euhedral to subhedral, and prismatic in shape. Oscillatory zoning is common, and some grains have different features, such as areas with high luminescence (Fig. 10D9). Zircon analyses form a scattered array on the concordia diagram. However, based on 11 more consistent results, it was possible to obtain a crystallization age at the upper intercept of 2062 ± 22 Ma (MSWD = 1.1, Fig. 5F). Nine zircon crystals produced predominantly positive values of $\varepsilon Hf_{(t=2.06Ga)}$, varying between 1.8 and -0.3, and the Hf-T_{DM}^{C} model age ranges from 2.7 to 2.5 Ga.

Whole rock Sm-Nd data

The results of Sm-Nd whole-rock analyses are listed in Table 3 and plotted in the εNd versus age diagram (Fig. 11). Four samples (EM-161A, EM-100, PR-143, and PR-165) were analyzed by U-Pb and Lu-Hf on zircon and Sm-Nd whole-rock methods. Seven additional samples (EM-13B, EM-22, EM-28, EM-33A, EM-115, PR-143, and PR-104) were only analyzed by Sm-Nd whole rock.

The $\varepsilon Nd_{(t)}$ values obtained are all negative (-0.88 to -9.68), and the ranges of the Nd-T_{DM} model ages vary between 2.35 and 3.05 Ga. From these data, it was possible to distinguish three groups. The first one is represented by Neoarchaean gneisses (A), followed by strongly deformed charnockitic rocks and Rhyacian granitoids (B), and the last group is represented by weakly deformed granitoids (C). In summary, considering the characterized rock, age of crystallization, lithostratigraphic unit, and Nd isotopic data, the samples of the study area were divided into the following three groups:

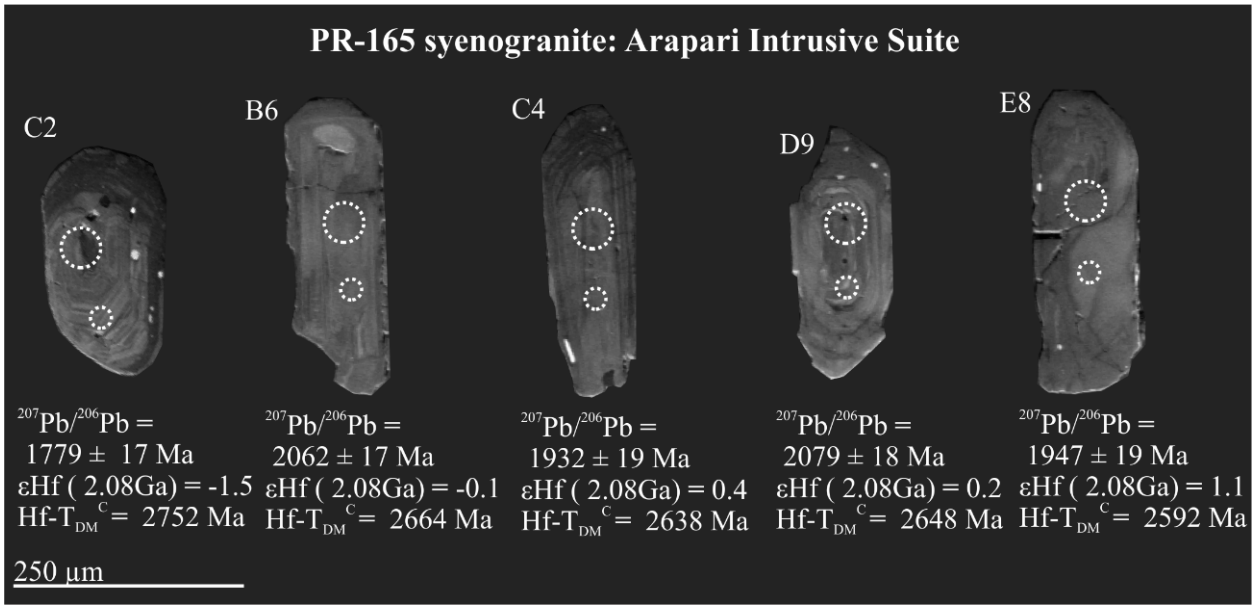

Figure 9. CL images of representative PR-165 syenogranite zircon grains from the Arapari Intrusive Suite. Circles indicate spot locations, the small ones being U-Pb and the large ones being Lu-Hf.

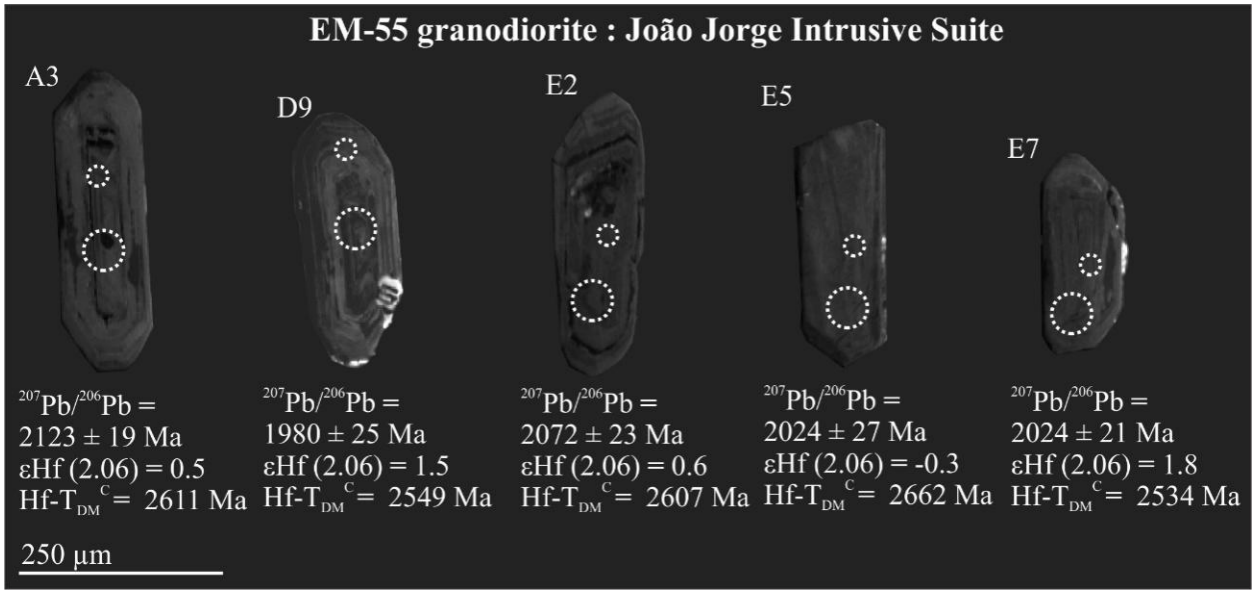

Figure 10. CL images of representative EM-55 granodiorite zircon grains from the João Jorge Intrusive Suite. Circles indicate spot locations, with the small ones being U-Pb, and the large ones being Lu-Hf.

- Neoarchaean gneisses (2.6 Ga) from the Aruanã Complex and the Tuerê Granulite yielded Mesoarchaean Nd-T_{DM} (3.05–2.98 Ga) and negative $\varepsilon Nd_{(t)}$ values between -3.08 and -2.95 (samples EM-13B and EM-161A);
- Deformed Rhyacian granitoids (2.10–2.06 Ga) from the Bacajaí Complex and the Arapari Intrusive Suite yielded Nd-T_{DM} at the Archaean limit (2.58–2.45 Ga) and negative $\varepsilon Nd_{(t)}$ values between -2.26 and -2.05 (EM-100, PR-165, and EM-115);
- Preserved Rhyacian granitoids (2.07 Ga) from the João Jorge Intrusive Suite yielded Nd-T_{DM} at the border of the Siderian period (2.35–2.36 Ga) and negative $\varepsilon Nd_{(t)}$ values between -1.45 and -0.88 (EM-22 and EM-28).

DISCUSSION

Crustal growth and Hf versus Nd tracers

Unraveling crustal evolution relies on isotope studies from whole-rock samples (more conventional, with widespread data) and single-grain zircon (which presents recent advances in analytical capabilities and a growing data acquisition on the Amazonian craton). In this study, samples were analyzed with both methods, for comparison and to elucidate the growth and differentiation of the continental crust.

The first and more obvious difference from both methods is that whole-rock samples show an overall dominant negative value ($\varepsilon Nd_{(t)}$) (Fig. 11) for rocks through all timespans analyzed. Single-grain zircon samples, however, comprise a more distinct

Table 3. Isotopic data of whole-rock Sm-Nd. Model ages were calculated based on the depleted mantle of DePaolo (1981).

Unit	Rock/Sample	Sm (ppm)	Nd (ppm)	$^{147}Sm/^{144}Nd$	$^{143}Nd/^{144}Nd$	f_{Sm-Nd}	$\varepsilon Nd_{(0)}$	Age (Ma)	$\varepsilon Nd_{(t)}$	T_{DM} (Ga)
Archaean gneisses and Granulites										
Aruanã Complex	Orthogneiss/EM 161A	14.19	83.81	0.10238	0.510845	-0.48	-34.98	[a]2630	-3.08	3.05
Tuerê Granulite	Orthogneiss/EM 13B	1.04	6.75	0.09314	0.510712	-0.53	-37.57	[b]2600	-2.95	2.98
-	Orthogranulite/PR 143	7.84	53.22	0.08907	0.511085	-0.55	-30.29	[a]2120	-1.46	2.41
Rhyacian granitoids and Charnockites										
Bacajaí Complex	Metatonalite/EM 100	4.18	20.91	0.12069	0.511481	-0.39	-22.57	[a]2103	-2.05	2.58
Arapari Intrusive Suite	Syenogranite/PR 165	9.73	52.4	0.11226	0.511366	-0.43	-24.81	[a]2080	-2.26	2.54
João Jorge Intrusive Suite	Granite/EM 22	13.37	90.45	0.08936	0.511130	-0.55	-29.42	[b]2070	-0.88	2.35
João Jorge Intrusive Suite	Granite/EM 28	9.26	74.84	0.07477	0.510902	-0.62	-33.86	[b]2070	-1.45	2.36
João Jorge Intrusive Suite	Granite/EM 33A	3.29	23.87	0.08341	0.510674	-0.58	-38.31	[b]2070	-8.23	2.79
Arapari Intrusive Suite	Syenogranite/EM-115	7.32	45.89	0.09647	0.511167	-0.51	-28.69	[b]2060	-2.19	2.45
Arapari Intrusive Suite	Syenogranite/PR 104	9.76	64.02	0.09212	0.510726	-0.53	-37.30	[b]2060	-9.68	2.93

[a]Ages obtained in this work; [b]source: Macambira and Ricci (2013).

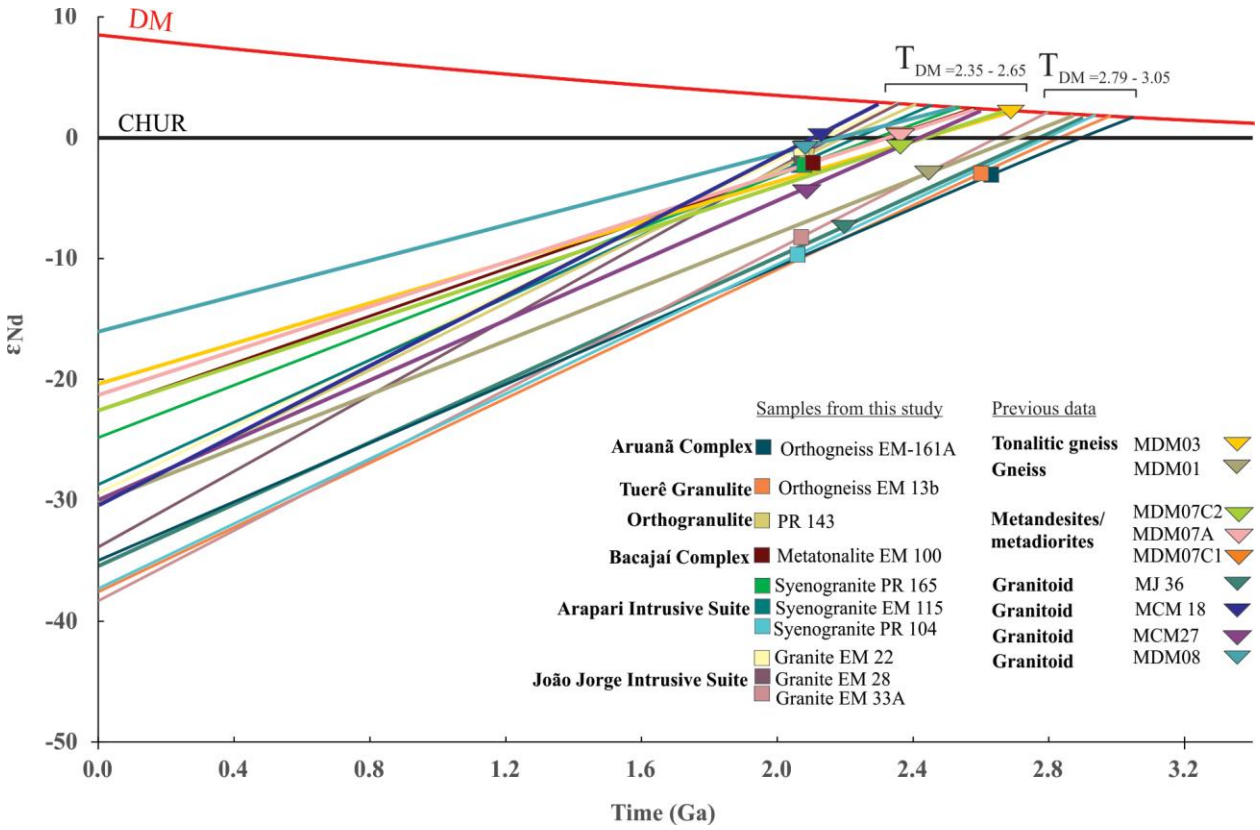

Figure 11. Diagram $\varepsilon Nd_{(t)}$ versus age (Ma) showing the evolution trends for the study samples. Previous data from Macambira *et al.* (2009).

pattern. Archaean registers are dominantly negative ($\varepsilon Hf_{(t)}$), and Rhyacian registers show a group of disperse values varying from negative to positive and another group (younger) with dominantly positive values (Fig. 12). Although the Lu-Hf single-grained zircon method has limitations, some authors (e.g., Scherer *et al.* 2007) concluded that they are more resistant to disturbance than Sm-Nd in whole rock and therefore have the potential to decipher the crustal growth history of highly metamorphosed terranes such as the BJD. From this comparison, Hf tracer on zircon enables deconvolution of intragrain isotope heterogeneity that might reflect complex growth histories (i.e., metamorphic overgrowths and inherited cores; unfortunately, in this work it was not possible to make such a distinction) or changes in the isotope composition of the melt from which the zircon precipitated in response to magma mixing or crustal assimilation in a more precise resolution than whole rock (this is corroborated with this work). Therefore, the crustal evolution for this region relies upon the zircon, yet the comparison with the whole rock is an important discussion for a better understanding of prior interpretations based on such data.

Archaean registers

Orthogneisses are strongly banded and show augen structure. NE-SW faults and foliations are identified by a new aero-geophysical project (CPRM 2016) that were formed prior to the Transamazonian cycle (Rhyacian magmatism covered this Archaean basement without continuity of such features) (Fig. 2). They yielded an igneous protolith age of 2.63 Ga (EM-161A) and a signature of a reworked crust (Hf-tracer). Those orthogneisses are correlated to the charnoenderbitic gneiss dated at around 2.60 Ga (Table 1) included in the Aruanã Complex (Vasquez *et al.* 2008c). Geochemical data of this unit point to a calcic-alkaline magmatism signature, suggesting a generation of volcanic arc in a continental margin (Macambira and Ricci 2013). Such data are, however, contrasting with the juvenile gneisses of the Manelão area (Macambira *et al.* 2009). Thus, two groups are possible to distinguish in the Neoarchaean: the first of 2.67 Ga is linked to island arc with the addition of juvenile crust, followed by a second of 2.63–2.60 Ga continental margin magmatism with crustal components.

Rhyacian magmatism and metamorphism

Rhyacian magmatism lasted ca. 40 Ma (2.10–2.06 Ga) and is divided into two magmatic periods. The first is represented by deformed granitoids included in the Bacajaí Complex (samples EM-100 and PR-170) that have crystallization ages between 2.1 and 2.09 Ga and show a significant spread in the

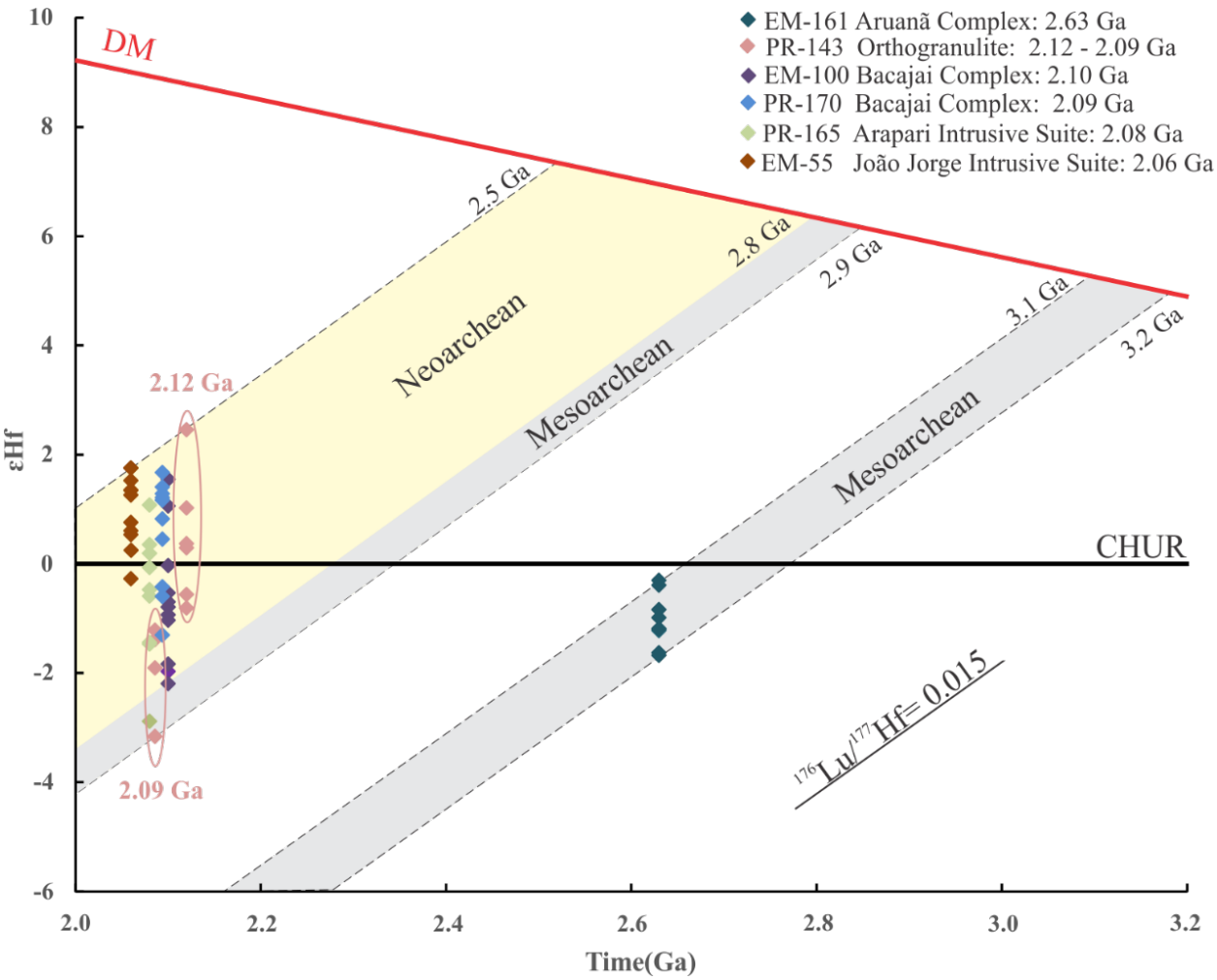

Figure 12. Evolution diagram, $\varepsilon Hf_{(t)}$ versus age (Ma) for the BJD studied units. The dotted lines represent crustal evolution trends, calculated using a $^{176}Lu/^{177}Hf$ of 0.015 for the average continental crust (Griffin *et al.* 2002, 2004). This diagram highlights the two distinct groups formed by the zircons from the Orthogranulite PR-143.

values of $\varepsilon Hf_{(t)}$ from negative to positive (some zircon crystals with $\varepsilon Hf_{(t)} = 0$, Fig. 12). The fact that some zircon crystals have a precise chondritic ($\varepsilon Hf_{(t)} = 0$) or slightly positive Hf composition at the time of crystallization is a solid evidence that they derive from mixed juvenile and crustal sources. Most granites have isotope signatures that preclude a direct mantle ancestry (for basic principles of partial melt), yet whole-rock samples show an overall negative signature for them as for the Rhyacian magmatism in this region. Thus, this points to a possible underestimated recognition of a new, mantle-derived material source (although mixed) in this magmatism.

At this same period, the orthogranulite (PR-143) yielded two concordant ages: 2.12 Ga and 2.09 Ga. Zircon crystals of these samples have irregular, chaotic zoning (Figs. 6D8 and 6D3) and zoning loss (Figs. 6A4 and 6C9), that according to Rubatto (2017), most of these features indicate metamorphic conditions of granulitic or anatexis facies. They also show a Th/U ratio variation of 0.32–0.91 (Table 4), out of some Th/U ratios range for metamorphic zircon < 0.1, although exceptions do exist as Vavra *et al.* (1996) attested. Most occurrences of metamorphic zircon with Th/U > 0.1 are from samples of high or ultra-high temperatures (> 900°C) (Vavra *et al.* 1996, Schaltegger *et al.* 1999, Moller *et al.* 2003, Kelly and Harley 2005), and this possibly indicates a high-grade temperature for the PR-143 sample. Orthopyroxene assemblages and the granoblastic texture also support a high metamorphic grade for this sample (Fig. 3). Otherwise, metamorphic zircon forms more easily in high-grade metamorphic rocks, where they commonly consist of overgrowths on inherited or detritic magmatic nuclei (Pidgeon *et al.* 2000). However, CL images obtained from the studied zircons do not distinguish metamorphic or igneous domains (Fig. 6), only a bright narrow rim not possible to analyze (< 25 μm). Although one can see that both ages of 2120 ± 4 Ma (n = 6) and 2086 ± 4 Ma (n = 4) were obtained from mainly concordant analytical points, many zircons are discordant (Fig. 5). Such discordance is possibly related to losses of lead due to metamorphic events and/or metamictization process. Moreover, the two distinct Hf signatures observed in this sample corroborate the existence of two separated ages. The highest age exhibits $\varepsilon Hf_{(2.12Ga)}$ = 2.5 to -0.8; Hf-T_{DM}^{C} = 2.7 to 2.5 Ga, and the lowest age shows $\varepsilon Hf_{(2.09Ga)}$ = -1.2 to -3.2; Hf-T_{DM}^{C} = 2.9 to 2.7 Ga. Taking these data into account, an alternative more plausible interpretation is that two-zircon crystallization moments are related to Zr-saturation pulses in the magmatic chamber. At an earlier stage, zircon from a first magma pulse was crystallized (at 2.1 Ga with a juvenile signature) and was then progressively contaminated or mixed with crustal components in a second pulse (at 2.09 Ga with a negative signature). Because only a single sample from orthogranulite with such features was studied, further data are needed for confirmation. Thus, this could be an example of a sample that could distinguish with more precision the two different sources (the juvenile and the mixed one).

The last magmatism period described is represented by granitoids formed at 2.06 Ga that show preserved magmatic texture. These granitoids are included in the João Jorge intrusive suites (EM-55) and yielded ages of 2062 ± 22 Ma, slightly negative-to-positive Hf-Nd signatures, and model ages (Nd-Hf-T_{DM}) that are mainly Siderian (ca. 2.3 Ga). Geochemical data presented by Macambira and Ricci (2013) for this unit is characteristic of an A-type (anorogenic) magmatism. Thus, those data suggest a less contaminated/mixed source for these rocks, probably related to the final stage of the Transamazonian cycle (the third stage, post-collisional), as already proposed by Vasquez *et al.* (2008b).

Table 4. U-Pb isotopic data in zircon from the northeastern Bacajá domain.

			Isotopic ratios							Ages (Ma)						
ID[a]	f_{206}[b]	Th/U[c]	$^{207}Pb/^{235}U$	1σ (%)	$^{206}Pb/^{238}U$	1σ (%)	Rho[d]	$^{207}Pb/^{206}Pb$[e]	1σ (%)	$^{206}Pb/^{238}U$	1σ (abs)	$^{207}Pb/^{235}U$	1σ (abs)	$^{207}Pb/^{206}Pb$	1σ (abs)	Conc.[f] (%)
EM-161A orthogneiss: Aruanã Complex																
A4	0.0038	0.18	4.44	1.21	0.24	0.71	0.59	0.14	0.98	1,378.9	9.8	1,720.0	20.8	2,164.7	21.2	63.7
B3	0.0040	0.36	5.81	0.86	0.27	0.57	0.66	0.16	0.65	1,543.9	8.7	1,948.5	16.7	2,410.7	15.6	64.0
B7	0.0008	0.58	9.09	0.74	0.40	0.47	0.63	0.16	0.58	2,176.9	10.2	2,347.5	17.4	2,499.3	14.4	87.1
C3	0.0015	0.34	3.45	1.04	0.19	0.65	0.63	0.13	0.81	1,132.0	7.4	1,514.9	15.8	2,100.5	17.1	53.9
C4	0.0038	0.92	11.34	1.02	0.48	0.61	0.60	0.17	0.82	2,521.2	15.4	2,551.6	26.0	2,575.9	21.1	97.9
C9	0.0003	0.63	12.02	0.79	0.49	0.57	0.72	0.18	0.55	2,552.9	14.7	2,606.0	20.7	2,647.5	14.5	96.4
D1	0.0004	0.70	12.22	0.80	0.50	0.62	0.78	0.18	0.50	2,607.5	16.2	2,621.2	20.9	2,631.8	13.2	99.1
D3	0.0003	0.67	11.40	0.74	0.47	0.47	0.64	0.17	0.57	2,499.3	11.8	2,556.1	18.9	2,601.5	14.8	96.1
D4	0.0104	0.27	10.02	1.38	0.42	1.29	0.93	0.17	0.49	2,279.4	29.4	2,436.4	33.6	2,570.3	12.7	88.7
E2	0.0018	0.71	11.63	0.79	0.49	0.61	0.78	0.17	0.49	2,552.4	15.7	2,575.2	20.3	2,593.2	12.8	98.4
E4	0.0079	0.68	10.61	1.20	0.45	1.09	0.91	0.17	0.51	2,401.9	26.1	2,489.5	29.9	2,561.7	13.0	93.8
E5	0.0002	0.45	10.50	0.97	0.44	0.84	0.86	0.17	0.50	2,354.7	19.7	2,479.6	24.1	2,583.6	12.8	91.1
E8	0.0010	0.65	9.12	0.94	0.38	0.77	0.82	0.17	0.54	2,087.6	16.0	2,350.0	22.0	2,586.2	13.8	80.7
E10	0.0006	0.79	8.73	0.82	0.39	0.58	0.70	0.16	0.59	2,102.1	12.1	2,310.7	19.1	2,500.4	14.8	84.1
F8	0.0008	0.63	10.39	0.76	0.45	0.33	0.44	0.17	0.68	2,403.6	8.0	2,470.0	18.7	2,525.1	17.2	95.2
F9	0.0008	2.16	12.02	1.00	0.49	0.76	0.76	0.18	0.66	2,580.6	19.6	2,606.2	26.2	2,626.2	17.3	98.3
G3	0.0009	0.70	11.15	1.02	0.47	0.87	0.85	0.17	0.54	,2462.1	21.3	2,535.9	25.8	2,595.5	13.9	94.9
H2b	0.0009	0.35	7.30	1.41	0.32	1.26	0.89	0.16	0.63	1,803.0	22.7	2,149.4	30.3	2,499.0	15.8	72.1

Continue...

Table 4. Continuation.

ID[a]	f_{206}[b]	Th/U[c]	Isotopic ratios							Ages (Ma)						
			$^{207}Pb/^{235}U$	1σ (%)	$^{206}Pb/^{238}U$	1σ (%)	Rho[d]	$^{207}Pb/^{206}Pb$[e]	1σ (%)	$^{206}Pb/^{238}U$	1σ (abs)	$^{207}Pb/^{235}U$	1σ (abs)	$^{207}Pb/^{206}Pb$	1σ (abs)	Conc.[f] (%)
H6	0.0081	1.20	10.39	0.82	0.44	0.32	0.39	0.17	0.75	2,371.7	7.6	2,469.7	20.1	2,551.4	19.1	93.0
I3	0.0080	0.41	3.40	1.49	0.20	0.88	0.59	0.13	1.20	1,155.5	10.2	1,504.7	22.4	2,038.2	24.4	56.7
I9	0.0187	1.19	11.63	0.98	0.49	0.73	0.75	0.17	0.64	2,556.4	18.7	2,575.0	25.1	2,589.6	16.7	98.7
PR-143 orthogranulite																
A3	0.0007	0.66	7.17	1.21	0.39	0.91	0.76	0.13	0.79	2,136.8	19.5	2,133.4	25.8	2,130.1	16.9	100.3
A4	0.0005	0.69	6.30	1.22	0.35	0.91	0.75	0.13	0.81	1,935.3	17.6	2,018.8	24.6	2,105.2	17.0	91.9
A5	0.0003	0.63	7.10	0.93	0.39	0.52	0.56	0.13	0.77	2,115.5	11.0	2,124.1	19.7	2,132.5	16.3	99.2
B2	0.0002	0.55	6.94	0.96	0.39	0.55	0.58	0.13	0.79	2,100.6	11.6	2,104.4	20.2	2,108.1	16.6	99.6
B9	0.0012	0.91	7.05	1.07	0.39	0.60	0.56	0.13	0.89	2,117.5	12.7	2,118.2	22.7	2,118.9	18.8	99.9
C2	0.0003	0.70	7.02	1.05	0.39	0.71	0.68	0.13	0.76	2,108.7	15.1	2,114.1	22.1	2,119.4	16.2	99.5
C4	0.0006	0.39	6.82	0.98	0.38	0.60	0.61	0.13	0.78	2,077.8	12.5	2,088.3	20.5	2,098.7	16.3	99.0
C6	0.0005	0.59	5.68	1.60	0.32	1.39	0.87	0.13	0.80	1,794.6	24.9	1,927.6	30.9	2,073.8	16.5	86.5
C9	0.0003	0.61	7.23	1.03	0.40	0.68	0.66	0.13	0.78	2,170.8	14.8	2,140.3	22.1	2,111.2	16.4	102.8
D2	0.0004	0.65	6.84	0.86	0.38	0.35	0.41	0.13	0.78	2,087.5	7.3	2,090.9	17.9	2,094.3	16.4	99.7
D3	0.0002	0.66	7.11	0.87	0.39	0.44	0.50	0.13	0.76	2,135.1	9.3	2,125.0	18.6	2,115.3	16.0	100.9
D4	0.0004	0.66	6.81	1.00	0.38	0.64	0.64	0.13	0.77	2,082.1	13.3	2,086.6	20.8	2,091.1	16.0	99.6
D8	0.0011	0.32	6.72	1.00	0.38	0.64	0.64	0.13	0.77	2,061.2	13.2	2,075.4	20.8	2,089.5	16.1	98.6
C5b	0.0015	0.54	6.76	1.11	0.38	0.80	0.72	0.13	0.77	2,070.7	16.5	2,080.2	23.0	2,089.6	16.0	99.1
E4	0.0004	0.78	5.74	1.54	0.33	1.34	0.87	0.13	0.76	1,816.8	24.4	1,936.9	29.9	2,067.9	15.8	87.9
E7	0.0006	0.67	7.52	0.87	0.42	0.43	0.50	0.13	0.76	2,241.7	9.7	2,175.0	19.0	2,112.7	16.0	106.1
E9	0.0004	0.64	6.51	1.30	0.36	1.06	0.82	0.13	0.74	2,004.8	21.3	2,047.1	26.6	2,090.0	15.5	95.9
F4	0.0036	0.66	7.09	0.82	0.40	0.32	0.39	0.13	0.75	2,167.2	7.0	2,122.4	17.4	2,079.3	15.6	104.2
F9a	0.0014	0.32	5.11	1.90	0.29	1.74	0.92	0.13	0.76	1,651.7	28.7	1,837.2	34.9	2,054.3	15.7	80.4
F9b	0.0018	0.50	7.10	0.86	0.40	0.44	0.51	0.13	0.74	2,160.0	9.5	2,123.5	18.3	2,088.3	15.5	103.4
G2	0.0006	0.33	5.80	1.33	0.33	1.09	0.82	0.13	0.75	1,836.1	20.1	1,946.0	25.9	2,065.0	15.6	88.9
G3	0.0026	0.78	6.46	0.94	0.37	0.51	0.54	0.13	0.79	2,042.3	10.5	2,040.4	19.3	2,038.5	16.2	100.2
G4	0.0011	0.61	6.49	1.10	0.37	0.80	0.73	0.13	0.75	2,015.1	16.0	2,045.2	22.4	2,075.7	15.7	97.1
EM-100 metatonalite: Bacajaí Complex																
A1	0.0176	0.26	6.64	1.70	0.38	1.11	0.65	0.13	1.29	2,055.8	22.8	2,064.4	35.2	2,073.0	26.8	99.2
A3	0.0186	0.18	2.96	1.84	0.20	0.98	0.53	0.11	1.56	1,168.2	11.4	1,398.4	25.8	1,769.2	27.6	66.0
B2	0.0157	0.27	4.50	1.59	0.27	0.69	0.44	0.12	1.43	1,522.9	10.6	1,730.5	27.5	1,991.7	28.4	76.5
B3	0.0038	0.24	6.23	1.68	0.36	0.95	0.57	0.13	1.39	1,972.3	18.8	2,008.7	33.8	2,046.4	28.4	96.4
C1	0.0025	0.32	5.33	1.50	0.31	0.68	0.45	0.13	1.33	1,730.0	11.8	1,874.1	28.1	2,037.8	27.2	84.9
C2	0.0055	0.30	5.02	1.75	0.29	1.05	0.60	0.12	1.40	1,654.2	17.4	1,822.5	31.8	2,020.7	28.2	81.9
C3	0.0029	0.30	3.22	1.82	0.21	0.80	0.44	0.11	1.63	1,219.8	9.7	1,461.8	26.6	1,833.4	29.9	66.5
D1	0.0006	0.51	6.88	1.68	0.38	1.07	0.64	0.13	1.30	2,064.9	22.1	2,095.6	35.3	2,125.9	27.6	97.1
A4	0.0041	0.32	6.54	2.18	0.37	1.47	0.67	0.13	1.61	2,036.0	29.9	2,051.1	44.8	2,066.4	33.4	98.5
A5	0.0117	0.38	2.32	2.75	0.16	2.04	0.74	0.11	1.84	959.6	19.6	1,219.8	33.5	1,714.9	31.6	56.0
C4	0.0051	0.25	3.12	2.81	0.21	2.09	0.74	0.11	1.88	1,229.8	25.6	1,437.5	40.3	1,759.8	33.0	69.9
C5	0.0155	0.37	2.68	2.39	0.18	1.57	0.66	0.11	1.80	1,078.6	16.9	1,321.8	31.6	1,741.3	31.4	61.9
E3	0.0023	0.05	3.25	2.36	0.21	1.75	0.74	0.11	1.58	1,211.7	21.2	1,470.0	34.7	1,865.8	29.5	64.9
F3	0.0142	0.18	3.46	3.16	0.21	2.01	0.64	0.12	2.44	1,252.0	25.1	1,517.2	47.9	1,909.7	46.5	65.6
G1	0.0047	0.27	6.79	2.45	0.37	1.32	0.54	0.13	2.07	2,027.0	26.8	2,084.3	51.1	2,141.4	44.3	94.7
H1	0.0013	0.31	7.10	2.38	0.39	1.04	0.44	0.13	2.13	2,121.4	22.1	2,124.1	50.5	2,126.7	45.4	99.8
I3	0.0032	0.26	5.40	2.66	0.31	1.43	0.54	0.13	2.24	1,737.6	24.8	1,884.2	50.0	2,049.8	45.9	84.8
F5	0.0031	0.26	7.01	2.64	0.39	1.42	0.54	0.13	2.22	2,106.4	30.0	2,112.6	55.7	2,118.5	47.0	99.4
J4	0.0075	0.31	2.22	3.61	0.16	2.30	0.64	0.10	2.79	965.1	22.2	1,187.9	42.9	1,620.0	45.1	59.6
J2	0.0049	0.16	8.09	2.97	0.45	1.67	0.56	0.13	2.46	2,379.2	39.6	2,241.6	66.5	2,118.3	52.0	112.3
PR-170 monzogranite: Bacajaí Complex																
A2	0.0071	0.34	7.00	1.39	0.39	1.00	0.71	0.13	0.98	2,138.1	21.3	2,111.1	29.4	2,084.9	20.4	102.5
B1	0.0028	0.52	7.00	2.06	0.39	1.05	0.51	0.13	1.77	2,144.1	22.5	2,111.5	43.4	2,079.9	36.7	103.1
B3	0.0252	0.69	5.39	1.80	0.32	1.21	0.67	0.12	1.34	1,793.3	21.7	1,883.6	34.0	1,984.6	26.5	90.4
B6	0.0160	0.50	5.02	2.27	0.31	1.55	0.68	0.12	1.66	1,720.2	26.7	1,822.7	41.4	1,941.9	32.2	88.6
C5	0.0063	0.33	7.68	1.76	0.43	1.05	0.59	0.13	1.42	2,287.8	23.9	2,194.4	38.7	2,108.3	29.9	108.5
D2	0.0220	0.56	4.18	1.94	0.25	1.49	0.77	0.12	1.24	1,428.3	21.3	1,670.2	32.5	1,989.2	24.8	71.8

Continue...

Table 4. Continuation.

ID[a]	f_{206}[b]	Th/U[c]	Isotopic ratios							Ages (Ma)						
			$^{207}Pb/^{235}U$	1σ (%)	$^{206}Pb/^{238}U$	1σ (%)	Rho[d]	$^{207}Pb/^{206}Pb$[e]	1σ (%)	$^{206}Pb/^{238}U$	1σ (abs)	$^{207}Pb/^{235}U$	1σ (abs)	$^{207}Pb/^{206}Pb$	1σ (abs)	Conc.[f] (%)
E2B	0.0333	0.36	6.45	1.69	0.35	1.14	0.67	0.13	1.25	1,956.9	22.3	2,039.4	34.5	2,124.0	26.6	92.1
E5	0.0298	0.09	5.61	1.49	0.32	0.93	0.62	0.13	1.16	1,771.7	16.4	1,918.4	28.5	2,080.9	24.2	85.1
E8	0.0523	0.38	2.08	2.13	0.15	1.17	0.55	0.10	1.78	911.9	10.7	1,141.1	24.3	1,607.5	28.5	56.7
F4	0.0195	0.60	7.24	1.87	0.42	1.36	0.73	0.13	1.29	2,253.5	30.6	2,141.5	40.1	2,035.8	26.2	110.7
F7	0.0693	0.84	2.15	2.14	0.15	1.47	0.69	0.10	1.55	907.2	13.4	1,165.7	24.9	1,684.1	26.0	53.9
G4	0.0165	0.41	7.29	1.08	0.41	0.46	0.43	0.13	0.98	2,227.1	10.3	2,147.5	23.2	2,072.3	20.2	107.5
G6	0.0169	0.46	4.97	1.77	0.30	1.35	0.76	0.12	1.14	1,671.4	22.5	1,814.5	32.1	1,983.0	22.7	84.3
H5	0.0299	0.40	6.10	2.13	0.35	1.60	0.75	0.13	1.41	1,930.3	30.8	1,990.2	42.3	2,052.9	28.9	94.0
I2	0.0246	0.17	6.65	0.99	0.37	0.46	0.46	0.13	0.88	2,011.2	9.2	2,066.5	20.4	2,122.1	18.6	94.8
I3	0.0544	0.22	2.83	1.47	0.19	0.97	0.66	0.11	1.11	1,100.5	10.6	1,363.9	20.1	1,804.6	20.0	61.0
I4	0.0228	0.22	6.61	0.92	0.37	0.34	0.37	0.13	0.86	2,027.8	6.9	2,060.7	19.0	2,093.8	17.9	96.9
H9	0.0255	0.61	6.37	1.27	0.35	0.84	0.66	0.13	0.95	1,938.4	16.2	2,028.5	25.7	2,121.5	20.1	91.4
I9	0.0591	0.19	1.65	2.66	0.12	2.33	0.88	0.10	1.29	728.8	17.0	990.3	26.4	1,625.7	20.9	44.8
J6	0.0474	0.20	2.61	1.70	0.17	1.28	0.76	0.11	1.11	1,011.6	13.0	1,303.4	22.1	1,822.4	20.2	55.5
PR-165 syenogranite: Arapari Intrusive Suite																
B6	0.0052	0.62	6.73	1.06	0.38	0.68	0.64	0.13	0.82	2,092.1	14.2	2,077.0	22.1	2,062.2	16.9	101.4
B7	0.0061	0.69	4.93	1.41	0.29	1.11	0.79	0.12	0.86	1,661.0	18.5	1,807.0	25.4	1,979.8	17.0	83.9
C2	0.0079	0.60	2.63	1.85	0.18	1.56	0.85	0.11	0.99	1,043.2	16.3	1,310.4	24.2	1,779.3	17.5	58.6
C4	0.0181	0.33	4.95	2.20	0.30	1.96	0.89	0.12	0.99	1,707.6	33.5	1,810.7	39.8	1,931.7	19.2	88.4
D9	0.0044	0.73	6.28	1.54	0.35	1.28	0.83	0.13	0.86	1,954.0	24.9	2,015.3	31.0	2,078.6	17.9	94.0
E8	0.0058	0.25	4.18	1.59	0.25	1.26	0.79	0.12	0.97	1,459.2	18.4	1,670.6	26.5	1,947.5	18.9	74.9
G3	0.0034	0.18	4.66	1.08	0.28	0.66	0.62	0.12	0.85	1,569.0	10.4	1,759.2	19.0	1,993.2	17.0	78.7
G5	0.0052	0.17	5.25	1.33	0.30	1.03	0.78	0.13	0.83	1,703.7	17.6	1,860.4	24.7	2,040.3	17.0	83.5
G10	0.0054	0.15	1.91	1.82	0.14	1.40	0.77	0.10	1.17	842.3	11.8	1,084.3	19.8	1,609.0	18.8	52.4
I3	0.0012	0.91	6.56	1.53	0.37	1.27	0.83	0.13	0.85	2,023.8	25.7	2,053.4	31.4	2,083.4	17.8	97.1
EM-55 granodiorite: João Jorge Intrusive Suite																
A1	0.0108	0.15	3.50	2.66	0.22	2.34	0.88	0.12	1.25	1,280.7	30.0	1,526.8	40.6	1,886.7	23.7	67.9
A3	0.0035	0.12	7.86	1.24	0.43	0.88	0.71	0.13	0.87	2,315.9	20.5	2,214.8	27.6	2,122.7	18.6	109.1
A7	0.0032	0.14	3.81	1.50	0.23	1.10	0.73	0.12	1.03	1,352.7	14.8	1,595.3	24.0	1,932.4	19.9	70.0
B1	0.0085	0.24	2.82	1.74	0.19	1.21	0.70	0.11	1.24	1,098.5	13.3	1,362.0	23.7	1,803.6	22.4	60.9
C4	0.0166	0.11	2.10	1.74	0.16	1.03	0.59	0.10	1.40	930.9	9.6	1,150.1	20.0	1,590.8	22.2	58.5
C5	0.0070	0.10	2.07	1.52	0.15	0.93	0.61	0.10	1.20	886.0	8.3	1,139.7	17.3	1,661.0	19.9	53.3
D1	0.0122	0.08	1.64	2.17	0.13	1.39	0.64	0.09	1.66	781.2	10.9	986.4	21.4	1,476.3	24.5	52.9
D6	0.0020	0.11	4.90	1.88	0.29	1.36	0.73	0.12	1.29	1,616.7	22.1	1,802.6	33.8	2,024.9	26.0	79.8
D9	0.0027	0.09	4.47	1.74	0.27	1.17	0.67	0.12	1.28	1,523.8	17.9	1,725.8	30.0	1,980.3	25.4	76.9
E1	0.0113	0.29	2.46	2.93	0.15	2.65	0.90	0.12	1.25	902.3	23.9	1,260.9	36.9	1,938.9	24.2	46.5
E1B	0.0071	0.13	2.28	2.00	0.17	1.24	0.62	0.10	1.57	990.7	12.3	1,207.5	24.1	1,619.1	25.4	61.2
E2	0.0036	0.16	6.47	1.58	0.37	1.10	0.70	0.13	1.13	2,011.9	22.1	2,041.6	32.2	2,071.7	23.4	97.1
E5	0.0065	0.20	5.07	2.40	0.29	1.98	0.82	0.12	1.36	1,665.8	33.0	1,830.7	44.0	2,023.8	27.5	82.3
E7	0.0028	0.16	6.08	1.80	0.35	1.34	0.74	0.12	1.21	1,951.5	26.2	1,987.0	35.9	2,024.1	24.5	96.4
E10	0.0011	0.10	2.89	1.76	0.20	0.93	0.53	0.10	1.49	1,178.5	10.9	1,379.9	24.3	1,706.9	25.5	69.0
F1	0.0071	0.16	8.89	1.12	0.49	0.29	0.26	0.13	1.09	2,580.4	7.4	2,326.7	26.1	2,111.0	22.9	122.2
F7	0.0029	0.14	8.49	1.71	0.46	1.33	0.78	0.13	1.07	2,431.0	32.3	2,284.3	39.0	2,155.5	23.2	112.8
G6	0.0028	0.22	3.27	1.63	0.22	0.92	0.56	0.11	1.34	1,288.9	11.8	1,473.0	24.0	1,749.3	23.5	73.7
G9	0.0062	0.15	4.06	1.53	0.25	0.76	0.50	0.12	1.33	1,446.9	11.0	1,646.5	25.2	1,911.7	25.4	75.7
H6	0.0015	0.04	2.55	1.99	0.17	1.47	0.74	0.11	1.35	1,029.3	15.1	1,285.5	25.6	1,743.7	23.5	59.0
I3	0.0040	0.26	3.89	2.25	0.24	1.72	0.77	0.12	1.44	1,393.8	24.0	1,611.3	36.2	1,908.5	27.5	73.0
J1	0.0034	0.15	6.42	2.40	0.37	2.17	0.90	0.13	1.04	2,020.5	43.8	2,034.4	48.9	2,048.4	21.3	98.6
J3	0.0041	0.08	2.30	2.22	0.14	1.96	0.88	0.12	1.06	860.5	16.8	1,213.2	27.0	1,910.5	20.2	45.0
J4	0.0176	0.09	1.39	3.62	0.09	3.38	0.93	0.11	1.30	573.6	19.4	884.0	32.0	1,769.3	23.0	32.4
J7	0.0053	0.12	12.57	1.79	0.70	1.52	0.85	0.13	0.95	3,421.2	52.1	2,647.9	47.5	2,100.8	19.9	162.9
J8	0.0008	0.07	4.50	2.11	0.27	1.87	0.89	0.12	0.97	1,529.8	28.6	1,730.4	36.5	1,982.2	19.3	77.2
J9	0.0136	0.04	6.42	1.32	0.37	0.93	0.70	0.13	0.94	2,019.2	18.8	2,035.0	26.9	2,051.0	19.3	98.4

[a]Identification of the zircon sample; [b]fraction of the nonradiogenic ^{206}Pb in the analyzed zircon spot, where $f_{206} = [^{206}Pb/^{204}Pb]c/[^{206}Pb/^{204}Pb]s$ (c = common; s = sample); [c]the Th/U ratio is calculated relative to GJ-1 reference zircon; [d]Rho is the error correlation defined as the quotient of propagated errors of $^{206}Pb/^{238}U$ and $^{207}Pb/^{235}U$; [e]corrected for mass-bias by normalizing to GJ1 reference zircon and common Pb using the model proposed by Stacey and Kramers (1975); [f]degree of concordance = ($^{206}Pb/^{238}U$*100 age)/($^{207}Pb/^{206}Pb$ age).

CONCLUSION

The northeastern portion of the BJD has a large Archaean register comprised in the Aruanã Complex. Orthogneisses with conspicuous banded structure were recognized, and zircon from them yielded ca. 2.6 Ga. Hf-Nd data suggest a reworked crust with a Mesoarchaean source. These data show two distinct coeval Mesoarchaean magmatism occurrences in the BJD. One in the central portion of the BJD with a juvenile signature located in a WNW-ESE transcurrent shear zone, and the other in the northern portion with a reworked signature and NE-SW faults and foliations.

The Rhyacian granitogenesis is dominant in the BJD and lasted about 40 million years (approximately 2.10–2.06 Ga). Deformed granitoids comprise metatonalites, monzogranites, and syenogranites with ca. 2.1 Ga. The overall Hf isotopic results show a spread on the values of $\varepsilon Hf_{(t)}$, between 1.8 and -2.9, which indicates a mainly mantle-derived magma that assimilated older crust. Hf-T_{DM}^{C} and Nd-T_{DM} model ages for the rocks from this and prior studies indicate a main period of mantle extraction and crust formation in the Neoarchaean (between 2.8 and 2.5 Ga), but younger Siderian sources were identified (Nd-T_{DM} of 2.45 Ga; EM-115). This stage on the Transamazonian cycle probably has an underestimated observed mantle-derived contribution for crustal growth, which becomes evident with modern single-grain zircon analysis. The same samples analyzed by whole-rock methods show an overall negative signature, as in many other previous studies. The orthogranulite zircons described with chaotic and irregular zoning exhibit two concordant ages and distinct Hf signatures that could represent distinct moments in the magmatic chamber, perhaps detailing the magmatic evolution. The highest age (2.1 Ga) is the crystallization, with a juvenile signature, and the lowest age (2.09 Ga) has contributions of crustal components. On the contrary, João Jorge suite, represented by preserved granodiorites formed at 2.06 Ga with an Hf-Nd model age of ca. 2.3 Ga, probably represents a late stage (post-collision stage) within the Transamazonian cycle.

ACKNOWLEDGMENTS

We thank CNPq for its financial support (Universal Project; grant 428287/2016-6), the MSc. Scholarship provided for the first author, and the research fellowship (Process 311452/2017-5) provided for the second author. Universidade Federal do Pará (UFPA) for English revision support from the PROPESP/UFPA (PAPQ program). We are very grateful to the Geological Survey of Brazil (CPRM) for their loan of samples, concession of geological information, and assistance with the SEM images. We take this opportunity to thank also professors Roberto Vizeu Pinheiro and Claudio Lamarão, both from the UFPA, and Dr Marcelo Vasquez from CPRM, for their assistance in this work. We acknowledge and thank the judicious work carried out by the anonymous reviewers.

ARTICLE INFORMATION

Manuscript ID: 20220068. Received on: 06 JAN 2022. Approved on: 05 MAR 2023.

How to cite this article: Magalhães L.B., Macambira M.J.B., Macambira E.M.B., Ricci P.S.F. 2023. Crustal growth in the northeast portion of the Rhyacian Bacajá domain, SE Amazonian craton, based on U-Pb, Lu-Hf, and Sm-Nd data. *Brazilian Journal of Geology*, **53**(2):e20220068. https://doi.org/10.1590/2317-4889202320220068

L.B.M.: Writing – original draft, Data curation, Formal Analysis, Investigation, Methodology. M.J.B.M.: Conceptualization, Supervision, Validation, Visualization, Writing – review & editing. E.M.B.M.: Resources (donation of rock samples). P.S.F.R.: Resources (donation of rock samples).

Competing interest: The authors declare no competing interests.

REFERENCES

Andersen T., Andersson U.B., Graham S., Aberg G., Simonsen S.L. 2009. Granitic magmatism by melting of juvenile continental crust: new constraints on the source of Paleoproterozoic granitoids in Fennoscandia from Hf isotopes in zircon. *Journal of The Geological Society*, **166**:233-247. https://doi.org/10.1144/0016-76492007-166

Barros C.E.M., Besser M.L. 2015. *Bacajá River Sheet SA.22-Y-D-IV*. Scale = 1:100.000. Belém: Geological Service of Brazil (CPRM). 1 map.

Barros C.E.M., Macambira M.J.B., Santos M.C.C., Silva D.C.C., Palmeira L.C.M., Sousa M.M. 2007. Padrões de deformação sin-magmática e idade em zircão (evaporação de Pb) de granitos paleoproterozóicos da parte leste do domínio Bacajá, província Maroni-Itacaiúnas. *Revista Brasileira de Geociências*, **37**(2):293-304.

Besser M.L. 2012. *Origem e evolução das rochas paleoproterozoicas da área Rio Bacajá, Pará, Brasil*. MS Dissertation, Universidade Federal do Paraná, Curitiba, 147 p.

Bouvier A., Vervoort J.D., Patchett P.J. 2008. The Lu-Hf and Sm-Nd isotopic composition of CHUR: constraints from unequilibrated chondrites and implication for the bulk composition of terrestrial planets. *Earth and Planetary Science Letters*, **273**(1-2):48-57. https://doi.org/10.1016/j.epsl.2008.06.010

Chu N.C., Taylor R.N., Chavagnac V., Nesbitt R.W., Boella R.M., Milton J.A., German C.R., Bayonb G., Burton K. 2002. Hf isotope ratio analysis using multi-collector inductively coupled plasma mass spectrometry: an evaluation of isobaric interference corrections. *Journal of Analytical Atomic Spectrometry*, **17**:1567-1574. https://doi.org/10.1039/B206707B

Cristo L.C.F. 2018. *Estudo petrográfico e isotópico (Pb-Pb, U-Pb e Sm-Nd) de rochas metavulcânicas, mineralizações auríferas e rochas granitoides relacionadas ao greenstone bel três Palmeiras, Volta Grande do Xingu, Domínio Bacajá, Pará*. MS Dissertation, Universidade Federal do Pará, Belém, 65 p.

DePaolo D.J. 1981. Nd isotopic studies: some new perspectives on Earth structure and evolution. *EOS*, **62**(14):137. https://doi.org/10.1029/EO062i014p00137-01

DePaolo D.J. 1988. *Neodymium isotope geochemistry:* an introduction. Berlin: Springer-Verlag, 187 p.

Faraco M.T.L., Vale A.G., Santos J.O., Luzardo R., Ferreira A.L., Oliveira M., Marinho P.A.C. 2005. Levantamento geológico da região ao norte da Província Carajás. In: Souza V., Horbe A.C. (eds.). *Contribuições à Geologia da Amazônia*. Belém: SBG, v. 4, p. 32-43.

Griffin W.L., Belousova E.A., Shee S.R., Pearson N.J., O'Reilly S.Y. 2004. Archaean crustal evolution in the northern Ylgarn Craton: U-Pb e Hf-isotope evidence from detrital zircons. *Precambrian Research*, **131**(3-4):231-282. https://doi.org/10.1016/j.precamres.2003.12.011

Griffin W.L., Wang X., Jackson S.E., Pearson N.J., O'Reilly S.Y., Zhou X. 2002. Zircon chemistry and magma genesis, SE China: in-situ analysis of Hf-isotopes, Pingtan and Tonglu igneous complexes. *Lithos*, **61**(3-4):237-269. https://doi.org/10.1016/S0024-4937(02)00082-8

Jackson S.E., Pearson N.J., Griffin W.L., Belousova E.A. 2004. The application of laser ablation-inductively coupled plasma-mass spectometry to in situ U-Pb zircon geochronology. *Chemical Geology*, **211**(1-2):47-69. https://doi.org/10.1016/j.chemgeo.2004.06.017

Kelly N., Harley S. 2005. An integrated microtextural and chemical approach to zircon geochronology: refining the Archaean history of the Napier Complex, east Antarctica. *Contributions to Mineralogy and Petrology*, **149**:57-84. https://doi.org/10.1007/s00410-004-0635-6

Ludwig K.R. 2003. *User's Manual for Isoplot/Ex Version 3.00:* A Geochronology Toolkit for Microsoft Excel, v. 4. Berkeley: Berkeley Geochronological Center, Special Publication, 70 p.

Macambira E.M.B., Ricci P.S.F. 2013. *Geologia e recursos minerais da Folha Tucuruí – SA.22-Z-C, State of Pará*. Scale = 1:250.000. Belém: CPRM – Geological Service of Brazil, 122 p.

Macambira M.J.B., Vasquez M.L., Silva D.C.C., Galarza M.A., Barros C.E.M., Camelo J.F. 2009. Crustal growth of the central-eastern Paleoproterozoic domain, SE Amazonian craton: Juvenile accretion vs. reworking. *Journal of South American Earth Sciences*, **27**(4):235-246. https://doi.org/10.1016/j.jsames.2009.02.001

Milhomem Neto J.M., Lafon J.M. 2019. Zircon U-Pb and Lu-Hf isotope constraints on Archaean crustal evolution in the Southeastern Guiana Shield. *Geoscience Frontiers*, **10**(4):1477-1506. https://doi.org/10.1016/j.gsf.2018.09.012

Mineral Resources Research Company (CPRM). *Projeto aerogeofísico Rio Bacajá:* relatório final do levantamento e processamento dos dados magnetométricos e gamaespectrométricos. Geology of Brazil Programme – PGB. Rio de Janeiro: Lasa Prospecções, 2016.

Moller A., O'Brian P.J., Kennedy A., Koner A. 2003. Linking growth episodes of zircon and metamorphic textures to zircon chemistry: an example from the ultrahigh-temperature granulites of Rogaland (SW Norway). *Geological Society of London, Special Publication*, **220**(1):65-81. https://doi.org/10.1144/GSL.SP.2003.220.01.04

Monteiro P.C. 2006. *Investigação do limite entre domínios geocronológicos da região do médio rio Xingu, Sudeste do Cráton Amazônico*. MS Dissertation, Universidade Federal do Pará, Belém, 104 p.

Patchett P.J., Tatsumoto M. 1980. A routine high-precision method for Lu-Hf isotope geochemistry and chronology. *Contributions to Mineralogy and Petrology*, **75**:263-267. https://doi.org/10.1007/BF01166766

Pidgeon R.T., Macambira M.J.B., Lafon J.M. 2000. Th-U-Pb Th–U–Pb isotopic systems and internal structures of complex zircons from an enderbite from the Pium Complex, Carajás Province, Brazil: evidence for the ages of granulite facies metamorphism and the protolith of the enderbite. *Chemical Geology*, **166**(1-2):159-171. https://doi.org/10.1016/S0009-2541(99)00190-4

Ricci P.S.F. 2006. Mineralogically bizarre charnockitoids of the Bacajá high-grade block (Pará): Decharnockitised and reemplaced plutons mistakenly confused with granitoids crystallized at shallower crustal levels. In: 9th Symposium of Geology of the Amazonia. *Expanded summaries*. SBG.

Rubatto D. 2017. Zircon: the metamorphic mineral. *Reviews in Mineralogy & Geochemistry*, **83**(1):261-295. https://doi.org/10.2138/rmg.2017.83.9

Slama J., Kosler J., Condon D.J., Crowley J.L., Gerdes A., Hanchar J.M., Horstwood M.S.A., Morris G.A., Nasdala L., Norberg N., Schaltegger U., Schoene B., Tubrett M.N., Whitehouse M.J. 2008. Plesovice zircon – a new natural reference material for U-Pb and Hf isotopic microanalysis. *Chemical Geology*, **249**(1-2):1-35. https://doi.org/10.1016/j.chemgeo.2007.11.005

Santos J.O.S. 2003. Geotectônica dos Escudos da Guiana e Brasil Central. In: Bizzi L.A., Schobbenhaus C., Vidotti R.M., Gonçalves J.H. (eds.). *Geologia, tectônica e recursos minerais do Brasil*. Texto, mapas e SIG. Brasília: Serviço Geológico do Brasil, p. 169-226.

Schaltegger U., Fanning M., Günther D., Maurin J.C., Schulmann K., Gebauer D. 1999. Growth, annealing and recrystallization of zircon and preservation of monazite in high-grade metamorphism: conventional and in-situ U-Pb isotope, cathodoluminescence and microchemical evidence. *Contributions to Mineral Petrology*, **134**:186-201. https://doi.org/10.1007/s004100050478

Scherer E.E., Munker C., Mezger K. 2001. Calibration of the lutetium-hafnium clock. *Science*, **293**(5530):683-687. https://doi.org/10.1126/science.1061372

Scherer E.E., Whitehouse M.J., Munker C. 2007. Zircon as a monitor of crustal growth. *Elements*, **3**(1):19-24. https://doi.org/10.2113/gselements.3.1.19

Soderlund U., Patchett P.J., Vervoort J.D., Isachsen C.E. 2004. The ^{176}Lu decay constant determined by Lu-Hf and U-Pb isotope systematics of Precambrian mafic intrusions. *Earth and Planetary Science Letter*, **219**(3-4):311-324. https://doi.org/10.1016/S0012-821X(04)00012-3

Souza V.S., Macambira M.J.B., Kotschoubey B. 2003. Idade de zircão do granito Felício Turvo, garimpo de ouro do Manelão, região do Bacajá (PA): implicações tectônicas. In: Simpósio de Geologia da Amazônia, 8. *Resumos*... Manaus.

Stacey J.S., Kramers J.D. 1975. Approximation of terrestrial lead isotope evolution by a two-stage model. *Earth and Planatery Science Letters*, **26**(2):207-221. https://doi.org/10.1016/0012-821X(75)90088-6

Tassinari C.C.G., Macambira M.J.B. 2004. A evolução tectônica do Cráton Amazônico. In: Mantesso-Neto V., Bartorelli A., Carneiro C.D.R., Brito Neves B.B. (Eds.). *Geologia do Continente Sul-Americano:* evolução da obra de Fernando Flávio Marques de Almeida. São Paulo: Beca, p. 471-485.

Thirlwall M.F., Anczkiewicz R. 2004. Multi dynamic isotope ratio analysis using MC-ICP-MS and the causes of secular drift in Hf, Nd and Pb isotope ratios. *International Journal of Mass Spectrometry*, **235**(1):59-81. https://doi.org/10.1016/j.ijms.2004.04.002

Vanderhaeghe O., Ledru P., Thiéblemont D., Egal E. Cocherie A., Tegyey M., Milési J.P. 1998. Contrasting mechanism off crustal growth: geodynamic evolution of the Paleoproterozoic granite-greenstone belts of French Guiana. *Precambrian Research*, **92**(2):165-193. https://doi.org/10.1016/S0301-9268(98)00074-6

Vasquez M.L. 2006. *Geocronologia em zircão, monazita e granada e isótopos de Nd das associações litológicas da porção oeste do Domínio Bacajá: evolução crustal da porção meridional da Província Maroni-Itacaiúnas – Sudeste do Cráton Amazônico*. PhD Thesis, Universidade Federal do Pará, Belém, 212 p. Available at: http://rigeo.cprm.gov.br/xmlui/bitstream/handle/doc/165/tese_marcelo_vasquez.pdf?sequence=1&isAllowed=y. Accessed in Oct, 2019.

Vasquez M.L., Macambira J.B.M., Galarza M.A. 2005. Granitóides transamazônicos da região Iriri-Xingu, Pará – novos dados geológicos e geocronológicos. In: Souza V., Horbe A.C. (eds.). *Contribuições à geologia da Amazônia*. SBG: Belém, v. 4, p. 16-31.

Vasquez M.L., Macambira M.J.B, Armstrong, R. 2008a. Zircon geochronology of granitoids from the western Bacajá domain, southeastern Amazonian craton, Brazil: Neoarchaean to Orosirian evolution. *Precambrian Research*, **161**(3-4):279-302. https://doi.org/10.1016/j.precamres.2007.09.001

Vasquez M.L., Macambira M.J.B., Armstrong R.A. 2014. High-grade metamorphism constrained by U-Pb SHIRIMP ages: an example of the Bacajá Domain, Amazonian Craton, Brazil. In: South-American Symposium on Isotope Geology, 9. *Abstracts*... São Paulo.

Vasquez M.L., Rosa-Costa L.T., Silva C.M.G., Klein E.L. 2008b. Compartimentação tectônica. In: Vasquez M.L., Rosa Costa L.T. (eds.). *Geologia e recursos minerais do Estado do Pará:* Geographic Information System – SIG: Texto explicativo dos mapas geológico e tectônico e de recursos minerais do Estado do Pará. Scale 1:1.000.000. Belém: Mineral Resources Research Company, p. 39-112. Available at: http://www.cprm.gov.br/publique/Geologia/Geologia-Basica/Cartografia-Geologica-Regional-624.html. Accessed on: Aug 20, 2019.

Vasquez M.L., Rosa-Costa L.T., Silva C.M.G., Ricci P.S.F., Barbosa J.P.O., Klain E.V., Lopes E.C.S., Macambira E.M.B., Chaves C.L., Carvalho J.M.A., Oliveira J.G.F., Anjos G.C., Silva H.R. 2008c. Unidades litoestratigráficas. In: Vasquez M.L., Rosa Costa L.T. (eds.). *Geologia e recursos minerais do Estado do Pará:* Sistema de Informações Geográficas – SIG: Texto explicativo dos mapas geológico e tectônico e de recursos minerais do Estado do Pará. Scale 1:1.000.000. Belém: Mineral Resources Research Centre, CPRM, p. 113-215. Available at: https://rigeo.cprm.gov.br/handle/doc/10443. Accessed on: Apr 3, 2019.

Vavra G., Gebauer D., Schmidt R., Compston W. 1996. Multiple zircon growth and recrystallization during polyphase Late Carboniferous to Triassic metamorphism in granulites of the Ivrea Zone (Southern Alps): an ion mocropobe (SHRIMP) study. *Contributions to Mineral Petrology*, **122**(4):337-358. https://doi.org/10.1007/s004100050132